DEVELOPING IONOMER DETECTION METHODOLOGIES FOR USE IN QUALITY CONTROL SYSTEMS IN THE MANUFACTURE OF CATALYST COATED MEMBRANES

by

D. Jacobsen

A thesis submitted to the Faculty and the Board of Trustees of the Colorado School of Mines in partial fulfillment of the requirements for the degree of Master of Science in Mechanical Engineering (Thermal Fluids division).

Golden, Colorado

Date _____

Signed: _____
D. Jacobsen

Signed: _____
Dr. J. Porter
Thesis Advisor

Golden, Colorado

Date _____

Signed: _____
Dr. J. Berger
Professor and Head
Department of Mechanical Engineering

ABSTRACT

Polymer electrolyte membrane fuel cells (PEMFCs) are on the verge of being produced at unprecedented levels as fuel cell vehicles (FCVs) and other renewable energy resources are set to drastically increase their market share; thanks largely to international campaigns championing climate science and a new wave of young activists and investors. In order to drive production cost and waste down, it is critical that quality control methods are in place that are capable of accurately and rapidly measuring key characteristics of the catalyst layer (CL) and membrane in real time as the CL is forming. While work done at the National Renewable Energy Laboratory (NREL) has pioneered several new methodologies for inline autonomous detection systems which are capable of 100% area scanning, a method for checking ionomer loading in the CL and mapping out its distribution in catalyst coated membranes (CCMs) has never been reported in literature. As the ionomer's distribution in the CL is critical to fuel cell efficiency, lacking an inline or even post production method to check that intended targets are being hit poses a significant risk to manufacturers.

Due to this, a series of non-destructive evaluation (NDE) techniques were chosen to evaluate their efficacy in detecting the ionomer in the precursor catalyst inks and resulting catalyst layers, in addition to ordering samples by increasing ionomer content. An initial literature review of Raman spectroscopy was conducted, and while promising in other cases, was not pursued further as CCM samples have been found to combust under typical Raman conditions. Capacitive imaging, a popular industrial NDE for detecting delamination in composites and subsurface infrastructure/damage in concrete, was investigated as it seemed a natural progression from cyclic sweep voltammetry (CV) and electrochemical impedance spectroscopy (EiS); both of which having been previously performed on Nafion/CCMs with mixed results. From basic numerical models it is shown that the measured variation in substrate thickness produces a signal greater than that which can be expected from the

Nafion loading variation in the CL. Fluorescence spectroscopy was performed on several batches of the commercial Nafion dispersion, D2020, which was found to fluoresce at a wavelength range that could not be explained by the presence of the solvent. As Nafion has known absorption peaks in the UV and IR, transmission UV and FTIR spectroscopy was performed on the catalyst inks and CCMs. It is shown that in the UV the spectra is dominated by carbon scattering; whereas in the IR, the substrate absorbs the light in the spectral range of interest completely.

Subsequent ATR-FTIR experiments were ultimately successful in detecting the ionomer in catalyst films and in ordering samples by ionomer content. It was found that it is possible to observe the catalyst layer forming in real time while monitoring solvent levels and the eventual Nafion polymerization. The ordering of samples by ionomer content was possible by taking advantage of an area of anomalous dispersion caused by the strong absorption peaks (CF_2 symmetric and asymmetric stretching) of Nafion and the Christiansen effect. Expanding on the study presented here is necessary for tuning the correlation presented into an accurate measurement of ionomer loading, along with translating the findings into an inline detection system; one which currently does not exist, but is surely needed.

TABLE OF CONTENTS

LIST OF FIGURES

LIST OF TABLES

LIST OF SYMBOLS

charge amplifier gain [volts/coulomb] . . . . . α

reference capacitor . . . . . C_{ref}

lock in amplifier gain . . . . . β

AV voltage signal amplitude . . . . . A_0

total effective capacitance C

thickness of layer j, made of component i . . . . . d_{ij}

free space permittivity . . . . . ϵ_0

complex permittivity of material i . . . . . ϵ_{ri}

effective plate area . . . . . A_{pl}

effective area of Nafion layer . . . . . A_n

effective area of platinum layer . . . . . A_{pt}

change in voltage across layer i . . . . . ΔV_i

absorption (UV) . . . . . $A(\lambda)$

sample spectra intensity (UV) . . . . . $I(\lambda)$

reference spectra intensity (UV) . . . . . $I_0(\lambda)$

dark reference spectra (UV) . . . . . $D(\lambda)$

path length difference in interferometer arms . . . . . Δl

integer number (of wavelengths shifted) . . . . . m

wavelength [nm] . . . . . λ

% transmission (IR) . . . . . $T(\nu)$

critical angle (to achieve TIR) . . . . . θ_c

index of refraction of surface i, dependent on wavenumber, ν . . . . . $n_i(\nu)$

wavenumber [cm^{-1}] . . . . . ν

absorbance (IR) . . . . . $a(\nu)$

sample spectra intensity (IR) . . . . . $I(\nu)$

reference spectra intensity (IR) . . . . . $I_0(\nu)$

Nafion absorption peak i . . . . . ni

water absorption peak i . . . . . wi

nPa absorption peak i . . . . . pi

standard deviation . . . . . σ

LIST OF ABBREVIATIONS

Intergovernmental Panel on Climate Change	IPCC
electric vehicles	EVs
fuel cell vehicle	FCVs
Polymer electrolyte membrane fuel cell	PEMFC
gas diffusion layer	GDL
catalyst layer	CL
n-propanol/n-propyl alcohol	nPa
isopropanol/iso-propyl alcohol	iPa
ionomer to catalyst dried weight ratio	I/C
gas diffusion electrode	GDE
catalyst coated membrane	CCM
roll-to-roll manufacturing	R2R
X-ray fluorescence	XRF
polytetrafluoroethylene	PTFE
capacitive imaging	CI
cyclic sweep voltammetry	CV
electrochemical impedance spectroscopy	EiS
membrane electrode assembly	MEA
volatile organic compounds	VOCs
fast Fourier transform	FFT

Fourier transform infrared (spectroscopy) . . . . . FTIR

infrared . . . . . IR

attenuated total reflection (-fourier transform infrared spectroscopy) . . . . . ATR(-FTIR)

total internal reflection . . . . . TIR

spray inks, with target I/C of $X.Y$ . . . . . SXY

blade inks, with target I/C of $X.Y$ . . . . . BXY

single side coated CCM, with target I/C of $X.Y$, made with SXY . . . . . CXY

ACKNOWLEDGMENTS

I would like to thank Dr. Peter Rupnowski, Dr. Brian Green, and Michael Ulsh at the National Renewable Energy Laboratory for investing in me and fostering my growth as a scientist, and Dr. Patrick Kohl, Dr. Scott Strong, and Dr. Jason Porter at the Colorado School of Mines for making it a reality. This project could not have been completed with out the endless support of my parents, Jeff & Jolene, Sue & Christian; friends, Dr. Peter Weddle, and of course, Isabella Mendoza.

Here at the end, I realize, it's only the beginning.

CHAPTER 1

MANUFACTURING A SOLUTION TO A GLOBAL PROBLEM, AN INTRODUCTION

To move forward, something must be left behind. And it is well documented elsewhere that since the industrial revolution, what is exceedingly left behind is an assortment of greenhouse gasses. Several movements have recently gained popularity and general acceptance, thanks largely to international acknowledgments such as the *Paris Agreement* and the rising popularity of young activists ascending to the global stage. That is not to say that compliance has been guaranteed, or in some cases even attempted; as the US alone has refused to enter into the *Paris Agreement*, killed an initiative to acknowledge the need to begin transitioning to zero-emission energy sources within the next ten years (*Green New Deal Resolution*), and has disputed climate science as a hoax by (Sen. James Inhofe) submitting a snowball into the public record on the senate floor.

These actions have become increasingly worrisome, as the United Nations body for assessing climate science, the Intergovernmental Panel on Climate Change (IPCC), recently provided a special report in 2018 on the impacts of reaching 1.5 °C above pre-industrial levels, [1]. The special report summarizes the increased risks of droughts, sea level rise, impact on biodiversity and ecosystems, etc. at +1.5 °C and emphasizes that these effects are increasingly catastrophic at +2.0 °C and above. What is perhaps more alarming is that these warnings can hardly be classified as new information, (though the warnings do become more dire with every successive year of inadequate controls put in place). *Nature* published an article a year earlier on the effect that increases of 1.5 degrees and above would have on glaciers in the high mountains of Asia, [2]; and an article published in 2009 linked global sea level and global temperature [3]. Even earlier, in 1970 a collection of articles were published discussing the global effects of pollution, [4]; and this is far from an exhaustive search of historical literature describing climate change.

It may be somewhat comforting to then realize that the adage "money is the strongest motivator" cuts both ways. The rising popularity of renewable energy and zero emission technology has bolstered the market, leading manufacturers to invest more heavily in renewable R&D. Looking specifically at vehicles, a huge increase in demand for electric vehicles has lead to the explosion in Tesla stock, breaking over $1,000 per share at the time of writing; and Ford announcing that not only is it re-imaging its iconic muscle car line into an all electric vehicle line, (*2021 Mustang Mach-E*), but also that it is working on bringing an all electric F-150 to market as seen in their viral marketing ad posted July 2019, (video titled: *All-Electric F-150 Prototype: Tows 1M+ Pounds ‖ F-150 ‖ Ford*). And it's not only electric vehicles (EVs) that are seeing this increase in demand. Toyota announced that they are expecting a demand increase for their fuel cell vehicle (FCVs), the Mirai, necessitating a ten fold increase in production post 2020, [5].

While electric vehicles' recharge times are continuously getting faster, one of the appeals of a fuel cell vehicle is that its refuel time is already nearly identical to that of common every-day gasoline vehicles. With "fuel" ranges for all three types of vehicles ideally coming in at around 300 miles, FCVs are poised to greatly increase their market share as a green alternative to traditional vehicles. This is the motivation for the following work described herein. Polymer electrolyte membrane fuel cells (PEMFCs, also known as proton exchange membrane fuel cells), which are typically used in vehicles as they are relatively low temperature fuel cells, are about to be manufactured in unprecedented amounts.

Broadly, PEMFCs convert hydrogen and oxygen into water in such a way that the electrochemical reaction can power an external load. Figure 1.1 shows a generalization of this process. First hydrogen gas is fed into channels just outside of the gas diffusion layer (GDL) of the anode. The GDL is an extremely porous layer of carbon support which allows gas to flow, while also allowing the conduction of electrons to the current collector; which in turn is typically a slab of conductive metal. The gas will then permeate into the catalyst layer (CL), which is a denser area of a carbon/catalyst network held together with the ionomer.

The ionomer is a long chain polymer, typically Nafion, which is electrically insulating while being ionically conductive. The membrane will be made of this same material. Here, inside of the CL, the gas will reach the boundary between the catalyst (platinum) and the ionomer (Nafion). At this boundary, the electrochemical potential across the membrane drives the proton forward, while the electrically insulating nature of Nafion does not allow the electron to pass. The platinum catalyst facilitates the necessary ionization, leaving the hydrogen ion free to cross the membrane, while the electron travels out of the matrix towards the current collector, as its electric potential is highest on this side of the membrane. This freed electron is then able to perform work as it travels through an external load to recombine on the other side of the membrane. On the cathode side, an almost identical process occurs in which oxygen gas is fed into similar channels just outside of the GDL, it diffuses into the CL where it combines with hydrogen atoms and electrons to form water[1].

From this general understanding, it should be clear that the distribution of Nafion in the CL is critical to the effective surface area of the triple phase boundary, which limits the number of reactions that can take place at any instant in time, and therefore is critical to overall fuel cell efficiency. And indeed, earlier studies have shown that both an over-abundance and a scarcity of Nafion lead to under-utilization of platinum [6], which is an expensive waste of a precious metal. Because of this, Nafion in the catalyst layer is the subject of an entire field of study on its own. Several groups have studied the Nafion-platinum interface interactions [7–14], and Nafion channel formation and morphology, [15–21]. Other groups have focused on membrane characteristics, using various spectroscopic techniques to observe water retention and transport [22–29], and recast membrane characteristics [30, 31].

Great care must be taken in the manufacturing process to achieve optimal CL coatings, and several quality control checks must be in place to limit the amount of defective units. The manufacturing process typically begins with the fabrication of the catalyst inks that will eventually become the catalyst layer. This can be done by weighing out pre-calculated

[1]For accounting purposes: $2H_2 \rightarrow 4H^+ + 4e^-$; $O_2 + 4e^- \rightarrow 2O^{2-}$; $4H^+ + 2O^{2-} \Rightarrow 2H_2O$.

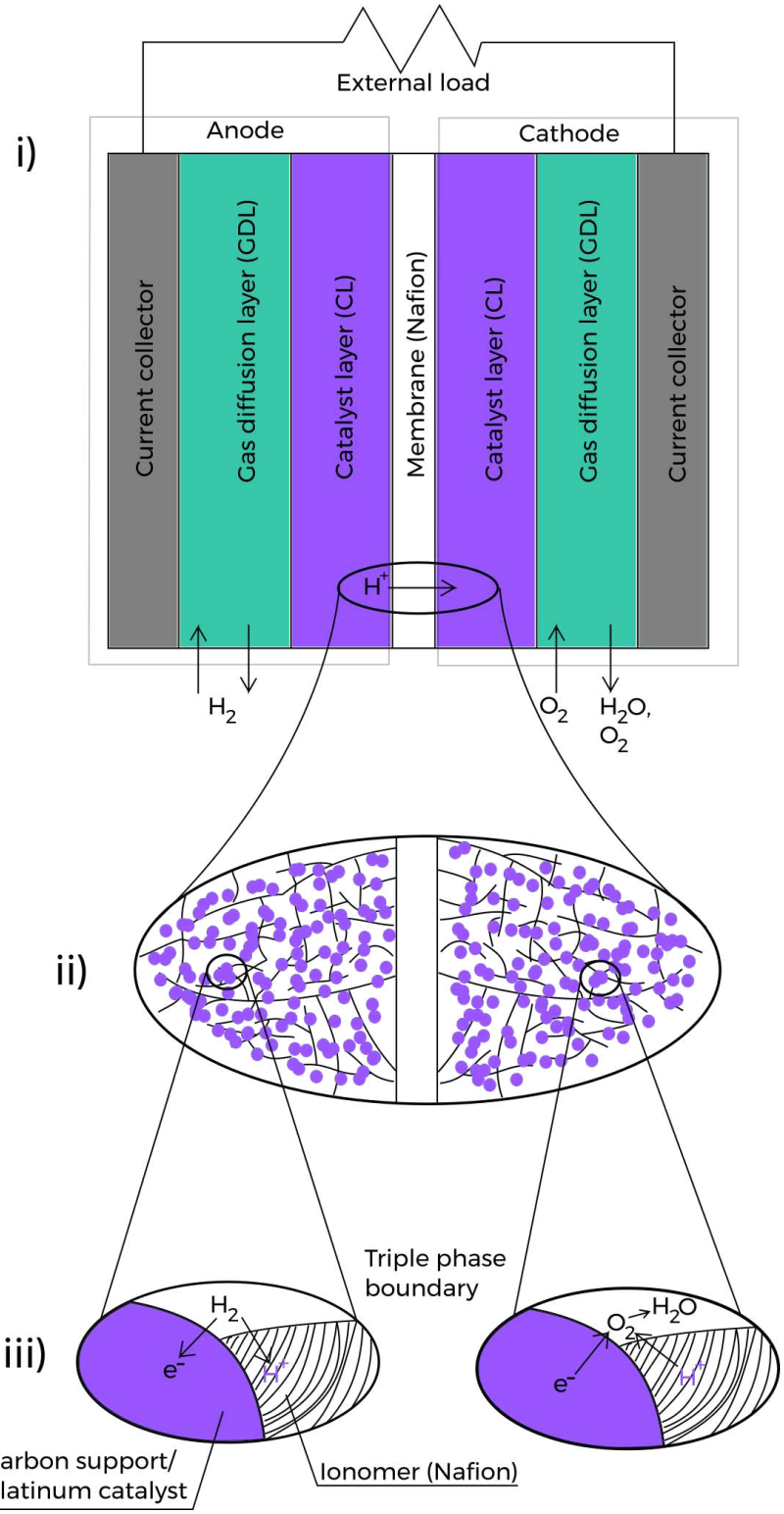

Figure 1.1: i) Generalization of fuel cell components. ii) depiction of carbon/catalyst/ionomer matrix inside of the catalyst layer. iii) Triple phase boundary where reactions occur.

amounts of carbon/Pt powder, D2020 (commercial Nafion dispersion in n-propanol and water), n- or iso-propanol (nPa/iPa), and water; and mixing them. The amounts of each component are calculated by desired batch volume and the desired ionomer to catalyst (I/C) ratio in the resulting catalyst layer. Thorough mixing can then be achieved by sonicating the slurry.

The next step in the process is then depositing the inks onto the substrate. The substrate can be the GDL forming what is known as a gas diffusion electrode (GDE), or the membrane forming a catalyst coated membrane (CCM). The focus of this work is on CCMs and the precursor inks, with only a passing reference to successful GDE studies. Regardless of the substrate choice, the remaining components from Figure 1.1 are hot-pressed together to form the fuel cell.

Scaling CCM production from laboratory tests to high throughput commercial mass production can typically be done via roll-to-roll (R2R) manufacturing, where hundreds of meters of Nafion membrane is unrolled at one end of the apparatus, coated in the catalyst ink, which is allowed to dry - forming the catalyst layer, before the now complete CCM is re-rolled at the other end. The coating techniques used include ultrasonic spraying, slot-die, and gravure coating [32]. It is here, before the CCMs are re-rolled, that inline quality control measures need to be implemented to minimize the risk of defective batches and the waste of precious materials.

Several non-destructive, inline measures have already been investigated. A machine vision technique was found to be effective in detecting pinholes, foreign particulates, and other defects that have settled in or on the membrane prior to coating [33–35]. A disadvantage of this method is that it does not provide certain information such as membrane thickness, which is a crucial aspect to the final fuel cell operation. To combat this, a new technique was developed and successfully demonstrated on commercial membranes of various thicknesses [36]. However, this technique similarly cannot be applied to catalyst layers, as they are opaque. This leaves the platinum loading of the samples to generally be checked post

production, on a per sample basis, using X-ray fluorescence (XRF) [37,38]. This is far from ideal, as high throughput testing post production using XRF is difficult to say the least. To get around this, a novel thermal imaging technique has been proposed at the National Renewable Energy Laboratory which would yield a thermal signal proportional to the platinum loading while also be amenable to inline implementation, if successful [39]. An effective method that would allow for the measurement of the ionomer concentration in the catalyst layer has not been reported. In practice, the target Nafion concentration is calculated during the ink fabrication stage, and there is generally no post production check to confirm that this target has been hit. The stated goal of this work is then to evaluate a series of NDE techniques on their efficacy in detecting the ionomer in the precursor catalyst inks and resulting catalyst layers, in addition to ordering samples by increasing ionomer content. This should form a solid basis from which to build a high throughput, inline detection system for quality control purposes.

CHAPTER 2

BACKGROUND AND OVERVIEW OF METHODS

2.1 Raman spectroscopy

An initial literature review was conducted investigating Raman spectroscopy after it was found that it was possible to measure polytetrafluoroethylene (PTFE) in a gas diffusion electrode (GDE). While successful in this effort, the process was time consuming and hard to scale [40, 41]. As PTFE is the polymer that makes up the repeating backbone of Nafion, and shares the two strongest absorbance features from CF_2 stretching [22], this mapping process may be translatable to Nafion in CCMs. However, directly applying this technique to CCMs is not as straightforward as it would appear, as a recent paper by Böhm et al. points out that the power associated with Raman spectroscopy burns the carbon black in the catalyst, destroying the Nafion with it, [42]. Because of this, research in this area has primarily focused on Raman on Nafion membranes, after the catalyst layer had been ablated away [42]; on platinum and carbon black powder to test the durability [43, 44]; and on graphene/ite [45–47] and platinum [14, 48] separately. As the focus of this work is on CCMs and the precursor inks, no further investigation was undergone.

2.2 Capacitive imaging

2.2.1 Background and theory

Capacitive imaging (CI) is a technique in which, traditionally, a set of planar plates, or series of planar plates, are moved with respect to a sample while an alternating current is passed to the plates. This current creates a quasi-static electric field between the plates, essentially making them a set or series of modified parallel plate capacitors. The capacitance of which can be modified by anything being placed near them due to the change in the dielectric constant of the material compared to air, or other materials around it [49–52].

Finite element analysis and other numerical models have been made to model capacitive imaging systems and their measurement sensitivity [53–55]. One such model was able to return the exact size, shape, and location of four cylinders placed over its surface, and even delamination between composite layers [53].

Capacitive imaging experiments have been performed on concrete, looking for cracks, rebar, and voids in the material [51]; and on composite materials looking for delamination of layers, impact damage, and identifying different subsurface liquids trapped in the structure [52,56]. Others have looked at CI on insulators [49,50], and at the process in general [57–61].

While capacitive imaging techniques have not yet been used in relation to polymers used in fuel cell application, it has been shown that there is a dependence on Nafion in two similar techniques, cyclic sweep voltammetry (CV) [62] and electrochemical impedance spectroscopy (EiS) [63, 64]. The latter directly correlates Nafion content to the capacitance of the cell. It is then feasible that a model could be created which would show the sensitivity of the CI system to slight changes in the Nafion content of the CCM.

2.2.2 Modeling ideal scenario

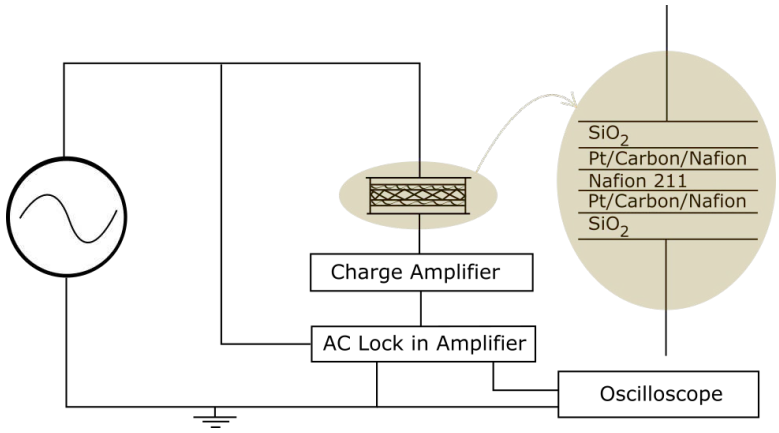

Figure 2.1: Capacitive Imaging setup inspired by work done by *Yin et al.*

The working model is based off the setup shown in [50–52]. In our model an AC current is passed to a parallel plate capacitor, where the plates have been coated in a silicon oxide

(SiO_2) and a CCM has been placed between the plates as a dielectric material. A charge amplifier (current integrator circuit) transforms the charge accumulating on the capacitor to an amplified AC voltage, which is then passed to an AC lock in amplifier which further amplifies the signal and outputs a DC voltage which can be read by a multimeter or oscilloscope, (cf. figure Figure 2.1).

The voltage amplitude that would be recorded should then follow

$$V_0 = \alpha\beta A_0 C \tag{2.1}$$

where α is the *charge gain* from the charge amplifier, which is equal to the inverse of the reference capacitor (C_{ref}) in the amplifier and has units of [volts/coulomb], β is the gain from the lock in amplifier and is unitless [-], A_0 is the amplitude of the input AC voltage signal having units of [V], and C is the total capacitance of the capacitor with the dielectric components inserted. Plugging the definition for α into equation (2.1) then gives

$$V_0 = \frac{\beta A_0}{C_{ref}} C \tag{2.2}$$

If it is assumed that C_{ref} and C are of the same order of magnitude, and that A_0 is of magnitude 1, then the output voltage is directly proportional to the gain from the lock in amplifier, which is advantageous, as C will undoubtedly be small. The equation that should govern C is given below[2]

$$C = \left(\frac{d_{s1} + d_{s2}}{\epsilon_0 \epsilon_{rs} A_{pl}} + \frac{d_m}{\epsilon_0 \epsilon_{rn} A_{pl}} + \frac{d_{n1} + d_{n2}}{\epsilon_0 \epsilon_{rn} A_n} + \frac{d_{pt1} + d_{pt2}}{\epsilon_0 \epsilon_{rpt} A_{pt}} \right)^{-1} \tag{2.3}$$

where d_{ij} corresponds to the thickness of the layers ($s \rightarrow SiO_2$, $m \rightarrow$ membrane, $n \rightarrow$ Nafion coated layer, and $pt \rightarrow$ platinum coated layer) assuming both the top and bottom of the membrane is coated (1 and 2 respectively), ϵ_0 is the free space permittivity (8.854×10^{-12} F/m), and ϵ_{ri} is the complex permittivity of the materials. Finally A_{pl} corresponds to the area of the plates, A_n corresponds to the effective area of the Nafion coating, and A_{pt} corresponds to the effective area of the platinum coating.

[2] A carbon layer has been excluded from the model in the interest of clarity. Further justification is presented later.

Mathematica was then used to plot equations (2.2) and (2.3) with values commonly found in literature as functions of A_n, A_{pt}, d_{nj}, and d_{ptj} as shown in Figure 2.2 - Figure 2.5. Figure 2.2 and Figure 2.4 show the response from an approximate 10% change in the variable in question while the other variables are held constant; and figures Figure 2.3 and Figure 2.5 show extended change in the variable being examined to show the non-linearity of the overall response of the system.

A previous electrochemical impedance spectroscopy (EiS) study had been conducted at NREL on membrane electrode assemblies (MEAs), and the initial work for that experiment found that the membranes (Nafion 212) varied in thickness from 34.2 - 36.8 μm [3]. Interchanging these values in the model produced a $\sim 4.6\%$ change in the output voltage. Therefore, any change in the output voltage of the model less than this produced by any of the variables will be lost to the noise inherent in the system. The lower value of 34.2μm was used for the rest of the analysis and to produce the figures.

It has been shown in [65–67] that the surface roughness of the electrodes in the capacitor strongly affect the capacitance of the capacitor. This effect is not taken directly into account with this model and is instead represented by a change in the "effective area" (A_n and A_{pt}) used. It is assumed that varying the area of the term representing the layer in question will capture a similar response as if the layer roughness effect had been properly modeled[4]. Changing the thickness of the layer will then represent changes in the loading of the component, (platinum or Nafion).

Using the model, a 10% change in the effective areas of Nafion and platinum produce a $\sim 1\%$ and $\sim 1.5\%$ change respectively, as shown in figure Figure 2.2. While this change is

[3] the *fuelcellstore.com/nafion-212* and *sigmaaldrich.com* reports the thickness of their Nafion 212 membranes as 50.8 μm, which is a large departure from the recorded values of this experiment. Nafion 211 membranes are reported to be half as thick, which still does not align with these recorded values. It is possible that the measuring technique used compressed the membrane.

[4] Two things to note: 1) "layers" here are representative of how the model was made, assuming that each component which makes up this capacitor system can be broken up into layers stacked on top of each other, when in reality, they are in a homogeneous mixture with each other. And 2) the surface is assumed to be rough as platinum nanoparticles with Nafion "glue" surrounding them are not assumed to be distributed in a "crystalline" repetitive matter, the surface of which would more likely be smooth.

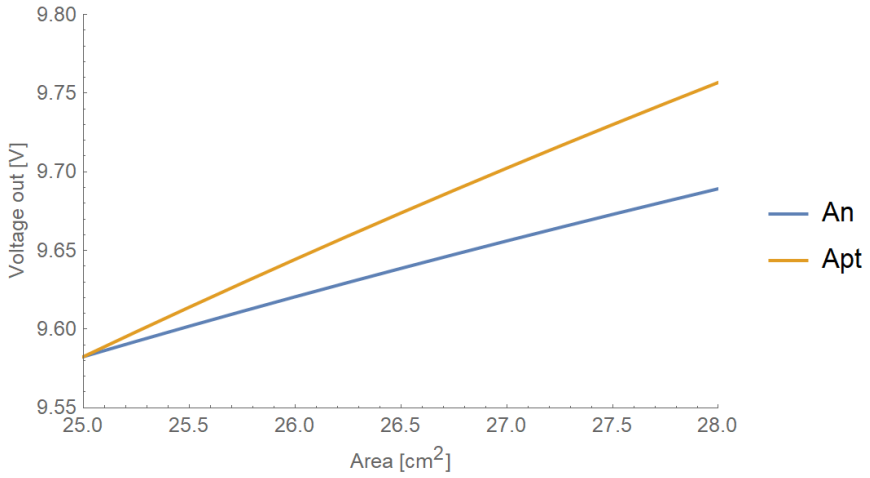

Figure 2.2: Voltage response of system with respect to changing effective area of platinum (Apt) and Nafion (An) separately.

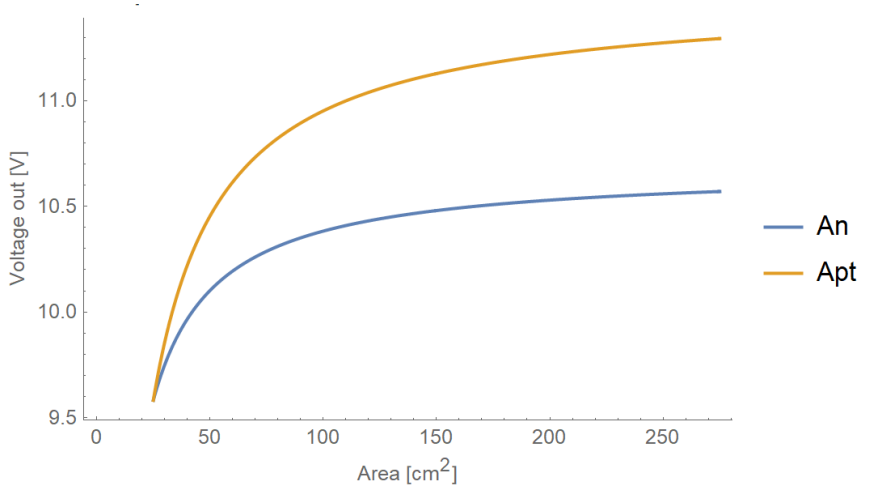

Figure 2.3: Voltage response of system with respect to changing effective area of platinum (Apt) and Nafion (An) separately, over extended areas to show non-linearity of response.

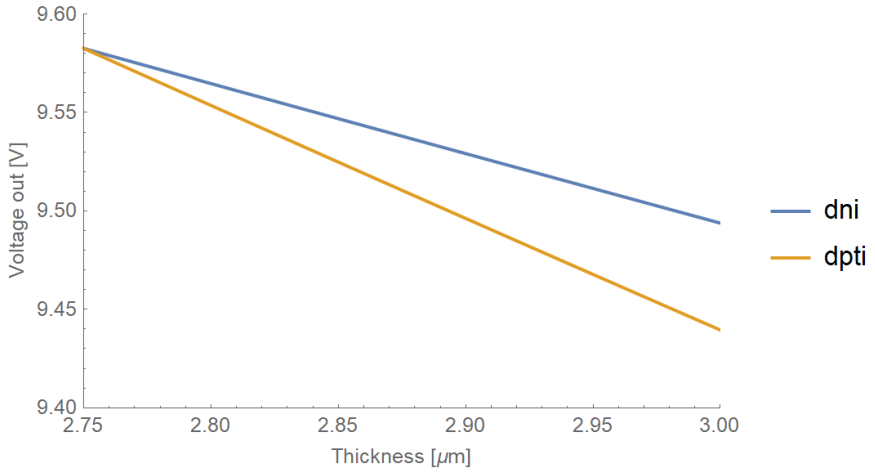

Figure 2.4: Voltage response of system with respect to changing the thickness of the platinum layer (dpti) and Nafion layer (dni) separately.

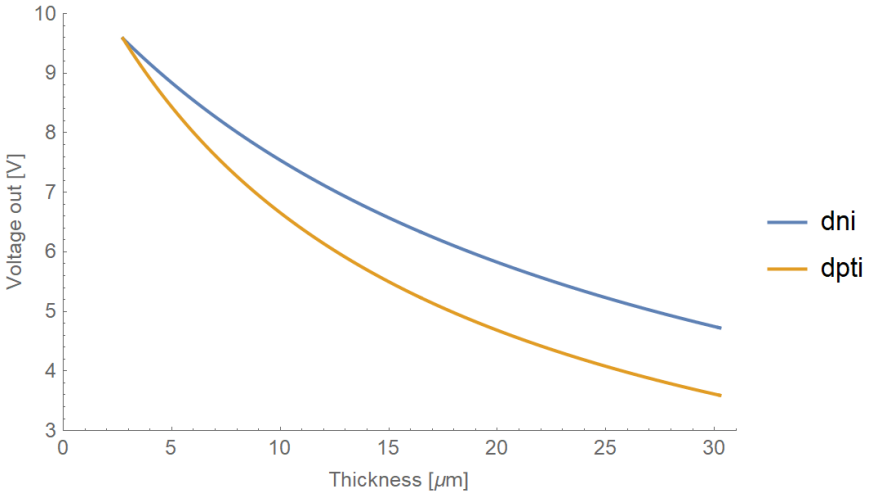

Figure 2.5: Voltage response of system with respect to changing thickness of the platinum layer (dpti) and Nafion layer (dni) separately, over extended distances to show non-linearity of response.

above the detection limit, ($\Delta V_{nafion} \approx 90mV$), neither change is above the noise produced by the difference in thicknesses of the membranes, (recall for any change to be significant, it must produce a change much larger than 4.6%).

Similarly, modeling a 10% change in layer thickness produced $\sim 1\%$ change from Nafion and a $\sim 1.6\%$ change from platinum, again, neither above the noise level.

It is possible to further refine the model, adding a carbon layer for completeness, (although it is likely that due to its conductivity that it would act only as a proportionality constant, multiplying the output voltage and leaving the % change untouched), and mathematically treating the catalyst layers as a mixture of components instead of separate layers. This can be shown by replacing equation (2.3) with (2.4).

$$C = \left(\frac{d_{s1} + d_{s2}}{\epsilon_0 \epsilon_{rs} A_{pl}} + \frac{d_m}{\epsilon_0 \epsilon_{rn} A_{pl}} + \left[\frac{\epsilon_0 \epsilon_{rn} (A_n/2)}{d_{n1}} + \frac{\epsilon_0 \epsilon_{rpt} (A_{pt}/2)}{d_{pt1}} \right]^{-1} + \left[\frac{\epsilon_0 \epsilon_{rn} (A_n/2)}{d_{n2}} + \frac{\epsilon_0 \epsilon_{rpt} (A_{pt}/2)}{d_{pt2}} \right]^{-1} \right)^{-1} \tag{2.4}$$

Another step would also be working towards better modeling the surface roughness effect properly, as shown in [68].

2.3 Fluorescence spectroscopy

2.3.1 Background and theory

Fluorescence spectroscopy is a popular and readily available tool, that if sensitive to Nafion loading, would be easy to implement into an inline system. The general concept of fluorescence can be seen in Figure 2.6. Simplified to the easiest case, if a sample has an electronic state whose energy is exactly equal to that provided by an incident photon, that photon will likely be absorbed. It then has a chance of undergoing a non-radiative transition to a lower state, afterwards it will relax back to the ground state by emitting a lower energy photon. The problem becomes significantly more difficult in more complex molecules as more transition states are possible along with the possibility of quenching.

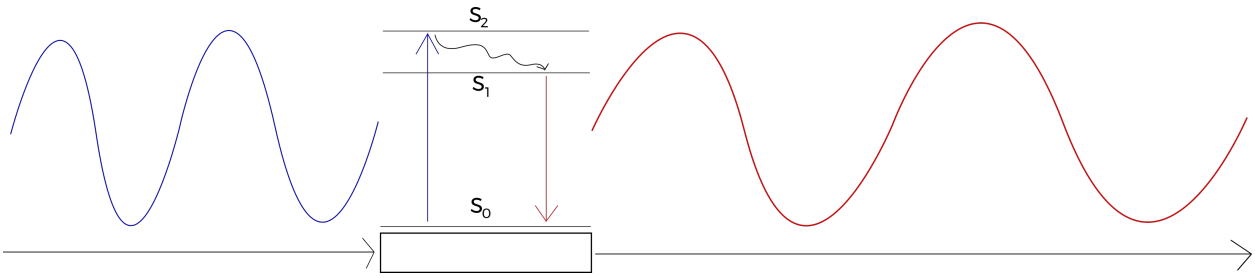

Figure 2.6: Jablonski diagram showing an incoming wave (blue) incident on a sample. The sample absorbs this photon, which excites the molecule up to a higher energy (S_2) electronic state from the ground (S_0) state. This molecule undergoes a non-radiative transition (black squiggle) down to the S_1 state; after which the the final relaxation to ground occurs, emitting a lower energy photon (red) in the process.

Several groups have already researched adding different fluorophores to Nafion to look at several different aspects, such measuring general fluorescence spectra of the tracers themselves introduced to the membrane/solution [69–73]; investigate Nafion hybrid films [74–76]; measuring the hydration [26, 77, 78] and transport/mobility of the water in the membranes [79]; and even linking the pH of a membrane to its water content via the fluorescence level of a tracer introduced to the membrane [80]. Something that's decidedly absent from literature is the fluorescence of Nafion itself. This section will discuss identifying Nafion fluorescence in D2020 and various inks used in the coating of CCMs.

2.3.2 Spectrofluorometer measurement

D2020 was diluted using MiliQ ultra-pure water to a 1:10 D2020 to water ratio. A Horiba Aqualog spectrofluorometer was used to record emission between 250-600 nm for excitation wavelengths between 200-600 nm. The emission was compared to a similarly prepared 1:10 solution of nPa and MiliQ water to isolate fluorescence from other components in the solution.

Figure Figure 2.7 illustrates the resulting contour plot produced by the Horiba Aqualog spectrofluorometer; with the excitation wavelength (Ex) along the x-axis, and emission wavelength (Em) along the y-axis. Each mapping is accompanied by its respective scale bar showing the relative intensity of the fluorescence. Figure Figure 2.7i shows that fluorescence

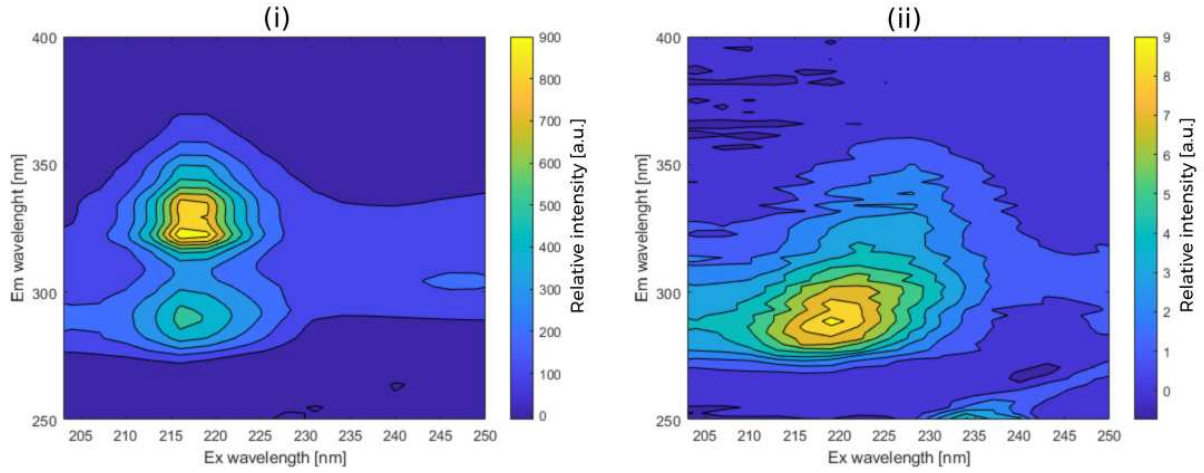

Figure 2.7: Fluorescence spectra collected for the 1:10 dilutions of (i) D2020 and (ii) nPa.

is observed around 325 nm at an excitation wavelength centered around 217 nm. This emission is decidedly absent from Figure 2.7ii. From the results, it is likely that one or more of the unlisted volatile organic compounds (VOCs) (reported to make up less than 1% by weight) are fluorescing; as Nafion has never been reported to fluoresce on its own, along with nPa and water being hereby ruled out. The experiment does not rule out further contamination in the dispersion. Repeating this experiment with different batches of D2020 provided similar results, signifying that a yet-to-be-identified component (likely one or more of the unlisted VOCs) common to several commercial Nafion dispersions fluoresce at low wavelengths. Water and nPa have been ruled out by comparing the recorded fluorescence individually; and Nafion has not been reported to fluoresce without the injection of a fluorophore.

A further expansion on this study is required to show whether or not the fluorescence scales consistently between different Nafion dispersions and subsequent dilution levels. If the fluorescence is near equivalent between different dispersions with the same Nafion concentration and scales well with dilutions, it may be that measuring the fluorescence off of a CCM will give a signal proportional to the surface level distribution of Nafion; despite the fact that the underlying fluorescence has not definitively been attributed to Nafion. Performing a quick back of the envelope calculation, assuming that the quantum yield is similar

to Tryptophan with a value of 0.14 [81] as Tryptophan is known to fluoresce over a similar wavelength range as observed here [82], the fluorescence signal that can be collected is reasonably approximated as

$$(\Phi_{Tryptophan})^2 \frac{A_{detector}}{4\pi r^2} \Rightarrow (0.14)^2 \frac{(2.5\text{E}^{-2})^2}{4\pi(0.3)^2} = 1.08\text{E}^{-3}\%$$

$1.08\text{E}^{-3}\%$ of the input power is likely to reach a 2.5×2.5 cm^2 detector 1/3 of a meter away. This also assumes that the resulting fluorescence is perfectly diffuse. With such a small value for the expected signal, the detection of Nafion on the surface of CCMs via fluorescence may not be possible for the same reason Raman spectroscopy was not investigated further; the input power required to get a usable signal may cause the CCMs to combust.

2.4 UV-Visible spectroscopy

2.4.1 Motivation

One of the easiest quality control methods to implement in R2R manufacturing is a simple line camera focused on the membrane. However, as the inks and CCMs are optically thick in the visible wavelength range, the information that can be ascertained from this method is severely limited, as mentioned earlier. This limitation can be somewhat circumvented by finding a wavelength at which Nafion absorbs, and observing intensity of the diffuse reflectance at that wavelength off of the surface of the CL. As UV light sources and detectors are abundant and relatively inexpensive, and the absorption spectra of Nafion in the UV is well documented elsewhere [83], UV-visible spectroscopy was performed, albeit in transmission, to evaluate the sensitivity to Nafion concentration that could be expected from this method.

2.4.2 Freestanding droplet method

An initial transmission study meant to be a proof of concept experiment was set up to focus a deuterium UV light source onto a drop of the liquid sample sitting on a mirror. The reflected light would then be focused into a fiber optic cable and passed to an Ocean Insight

Maya2000 pro series UV-Visible spectrometer (a diffraction grating spectrometer with a resolution of 0.24 nm and spectral range of 165-615 nm). It was found that the surface tension of the liquid samples caused a lensing effect, which saturated the detector. This lensing effect also changed continuously as the alcohol in the solutions evaporated, noted by the changing width of saturation present in the spectra. The experiment was therefore ended prematurely without collecting any spectra and labeled inconclusive.

2.4.3 Transmission study

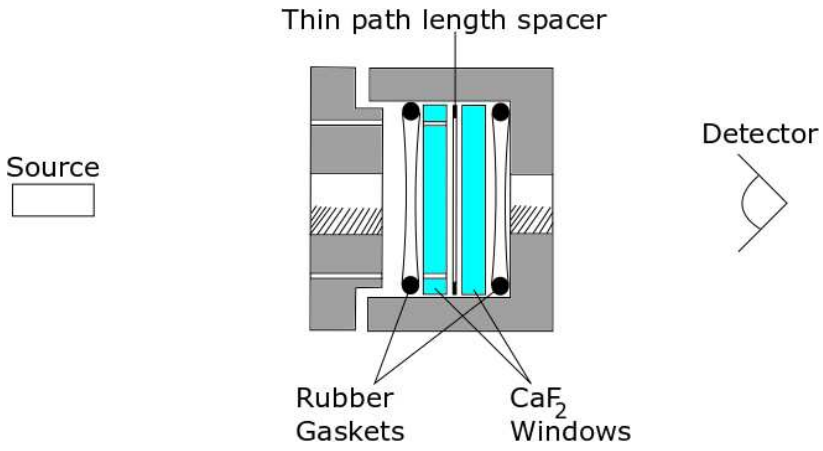

Figure 2.8: Cross section of the transmission cell assembly used to take liquid measurements.

Using the same deuterium light source and Ocean Insight spectrometer, transmission measurements of inks were taken using a Specac liquid transmission cell with CaF_2 windows initially spaced 0.2 mm apart. A cross section of this cell is provided in Figure 2.8. Between each measurement the cell was flushed with iPa. Transmission measurements of CCMs were also taken by hanging them in the path of the detector. These transmission measurements were then converted into absorption measurements by

$$A(\lambda) = 1 - \frac{I(\lambda) - D(\lambda)}{I_0(\lambda) - D(\lambda)} \tag{2.5}$$

where $I(\lambda)$ is the intensity of the light across the spectral range with the sample in place, $I_0(\lambda)$ is without any sample, and $D(\lambda)$ is the dark signal that the detector reads without the source being on. Performing this operation produces Figure 2.9 and Figure 2.10. From

Figure 2.9 it is clear that the CCM specimens and the catalyst inks are virtually opaque, and essentially indistinguishable from one another, across the entire spectral range. Plotting the absorption spectrum of a Nafion membrane alongside these spectra serves to show that the absorption features of the Nafion in the ink dispersions, and even the Nafion substrate of the CCMs themselves, are completely obfuscated. Two more inks were fabricated with the standard volume of Nafion added to produce a 0.9 I/C ink, only now with $1/5^{th}$ and $1/25^{th}$ the mass of carbon/pt added to the dispersions. The absorption spectra of these inks are added to produce figure Figure 2.10, confirming that carbon scattering is the main factor in obfuscating the Nafion absorption signal, and the overall opacity of the inks. Though, even with only $1/25^{th}$ of the carbon, Nafion features are still not clearly present in the spectrum.

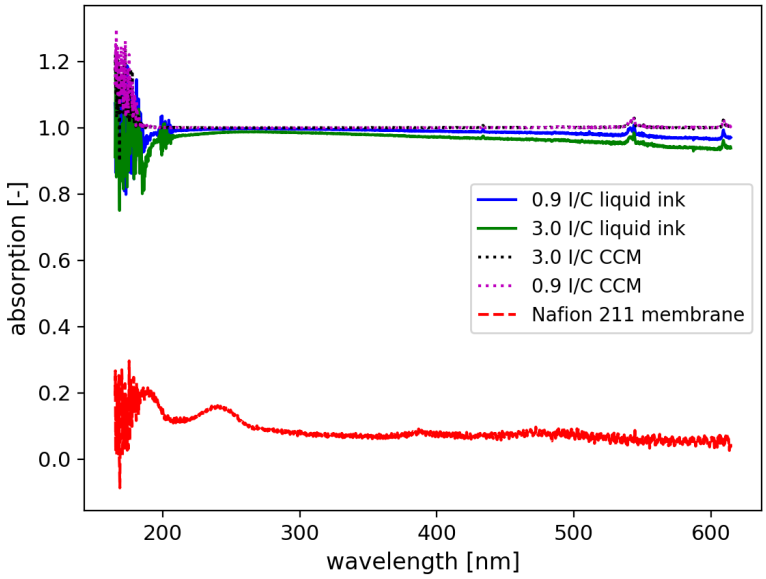

Figure 2.9: UV absorption, A, for Nafion 211 membrane, and 0.9 & 3.0 I/C inks and CCMs.

Subsequent measurements were performed with 0.9 and 3.0 I/C CCMs with differing platinum loadings and even a doubling up of the Nafion substrate. No meaningful change was observed in the resulting spectra, all CCM spectra were similarly opaque. During the disassembly of the transmission cell, it was observed that the flushing did not adequately

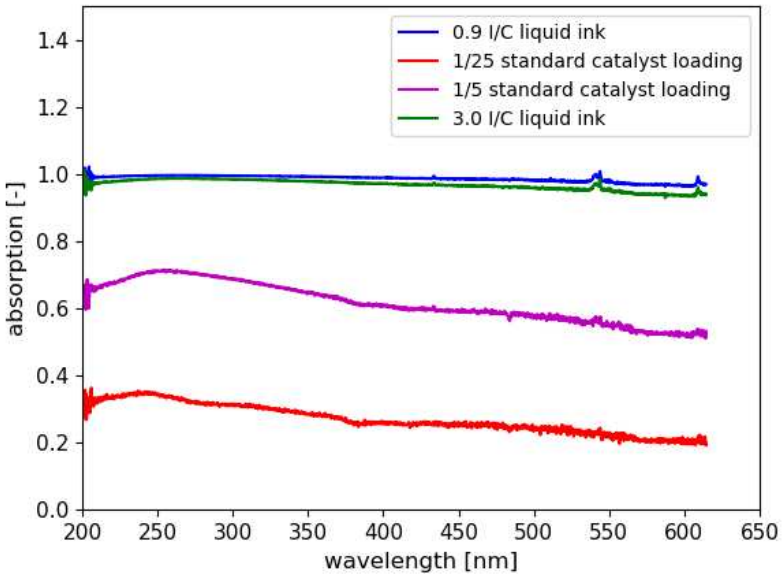

Figure 2.10: UV absorption, A, spectra for various inks using the flow method

clean the cell. Because of this and the opacity issue, the inks were retested with a window spacing now of 0.025 mm; and instead of flushing the cell, it was disassembled after every measurement to be more thoroughly cleaned. The resulting spectra showed a decrease in opacity, a drastic increase in variability between repeated measurements, but no significant difference between spectra could be attributed to changes in ionomer content alone.

Therefore, while the Nafion absorption reported in literature has been confirmed here, the presence of carbon in the inks and CCMs completely eclipses this absorption. It has yet to be seen whether this holds true for diffuse reflection off of the surface of a CCM. As the solvents making up $> 90\%$ of the inks are completely evaporated during the formation of the CL, thereby increasing the relative concentration of Nafion present, a diffuse reflection measurement may inherently be more sensitive to changes in ionomer concentration; however the collection of enough diffuse light to take said measurement poses its own challenges.

2.5 Fourier Transform Infrared (FTIR) spectroscopy

2.5.1 background and theory

A natural follow-up to UV spectroscopy is then IR spectroscopy, for many of the same reasons. The absorption peaks present in Nafion are very well documented [15, 84–86], and there exists a wealth of previous studies using Fourier transform infrared spectroscopy to investigate several aspects of Nafion and its role in PEMFCs [7–13, 22, 24, 28, 87–91]. Fourier transform infrared spectroscopy offers several advantages over traditional IR spectrometers which use diffraction gratings, such as the ability to collect spectra over a huge wavenumber range with great resolution, due to the way that the Fourier transform maps the spacial domain into the frequency domain. Because of this, FTIR was selected as the most appropriate method to further probe the inks and CCMs.

The hardware of an FTIR spectrometer can be simplified to a broadband IR light source, a Michelson-Morley interferometer, and a detector sensitive to this broad range of wavelengths. A simple schematic of what this setup could look like is provided in Figure 2.11. For a single wavelength, as the translation mirror moves a unit dx in x, the path length difference that the light must travel is $\Delta l = 2dx$. When this path length difference is integer multiples of the wavelength the light will undergo constructive interference, ($\Delta l = m\lambda$). Similarly, when the path length difference is the quantity of an integer plus a half multiplied by the wavelength, the light will undergo destructive interference, ($\Delta l = (m + 1/2)\lambda$), and ideally be perfectly dark. As the mirror travels, the intensity of light that reaches the detector should oscillate between these two extremes. When adding in additional wavelengths, this interference becomes more complex with different wavelengths destructively interfering at different distances x. The spectrometer works then by recording the intensity of the light that reaches it as a function of mirror position. The result is an interferogram with a maximum at zero path length difference. The spectrometer performs a fast Fourier transform (FFT) on the interferogram to convert it into intensity as a function of frequency, followed by a relatively straightforward conversion to get from frequency to wavenumber.

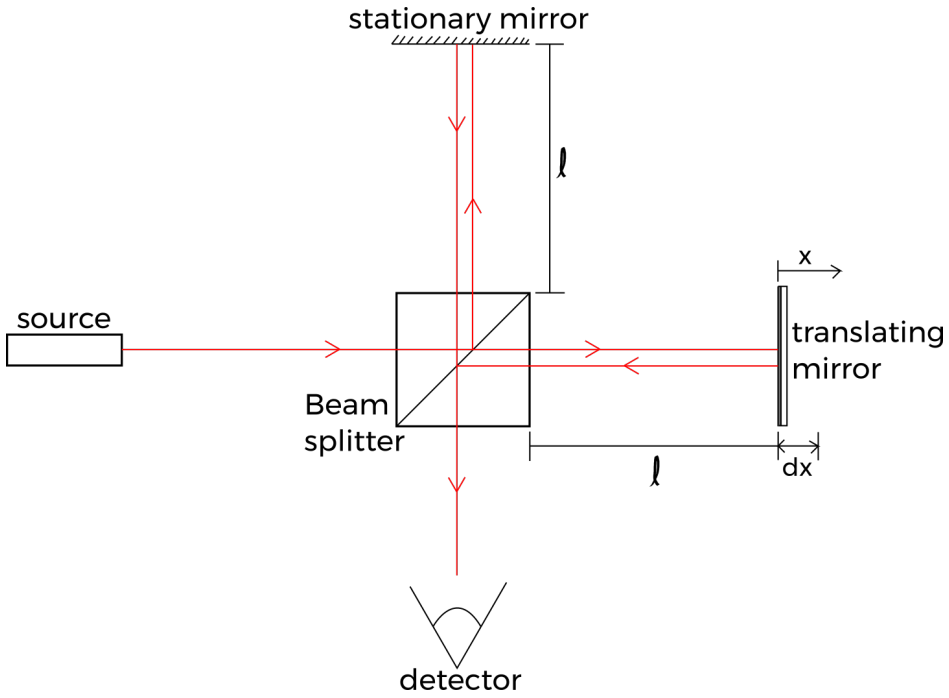

Figure 2.11: Simple Michelson-Morley interferometer.

Measuring the absorption of a substance can then be achieved by placing a sample between the detector and the beam splitter. Similar to the phenomenon described in Figure 2.6, if the sample has the capacity to store certain quantized units of energy, it will absorb that packet of energy. For polymers this energy is stored in the bonds between atoms which display as a stretching of that bond; with the quantized units of energy relating to the bond strength. Figure 2.12 depicts the Nafion polymer with the bonds responsible for the strongest absorption peaks highlighted and labeled. With the sample in place, the detector will record a new interferogram. Performing the same FFT operation, we can transform the resulting intensity plots into % transmission by

$$T(\nu) = \frac{I(\nu)}{I_0(\nu)} \tag{2.6}$$

where $I(\nu)$ is the intensity with the sample present, and $I_0(\nu)$ is that without.

An absorption measurement can be taken with relatively minor modification to the existing setup. A popular method is attenuated total reflection (ATR), which takes advantage of

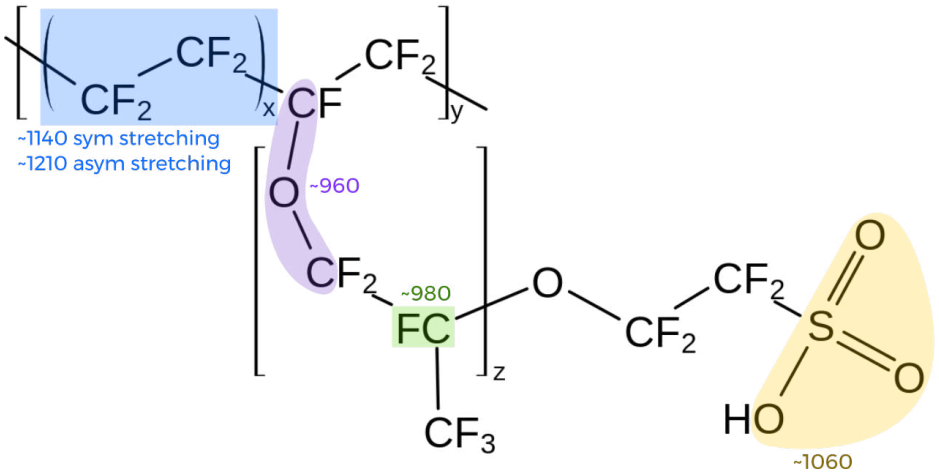

Figure 2.12: Drawing of Nafion polymer highlighting bonds responsible for absorption at the given wavenumbers [cm^{-1}]. *Underlying photo credit to Roland1952 submitted to public domain March 2009. Absorption assignments taken from [15, 84]*

the total internal reflection at an interface between something with a high index of refraction into something with a relatively lower index of refraction at an angle above the critical angle. The critical angle is that which solves Snell's law for an exit angle of $\geq 90°$, or

$$\theta_c = \sin^{-1}\left(\frac{n_1(\nu)}{n_2(\nu)}\right) \tag{2.7}$$

At this angle and above, the Poynting vector runs along the surface of the interface and the totality of the energy of the light is ideally reflected back into the material. At the point of reflection, energy is temporarily stored in a standing wave that is exponentially decreasing spacially as it extends deeper into the other material. This standing wave is known as an evanescent wave, and typically only extends a few microns in most ATR-FTIR applications, as it depends on ν and n. The trick then is to leach the energy from this standing wave by pressing a substance with a lower index of refraction against that surface, but who also absorbs within the spectral range of the incident light. An example of what this setup could look like is provided in Figure 2.13. By placing this attachment between the detector and beam splitter, an absorbance measurement can be made by the following Beer-Lambert law[5],

[5]Absorbance was calculated using log base e, or natural log, as opposed to log base 10.

$$a(\nu) = -ln\left(\frac{I(\nu)}{I_0(\nu)}\right). \tag{2.8}$$

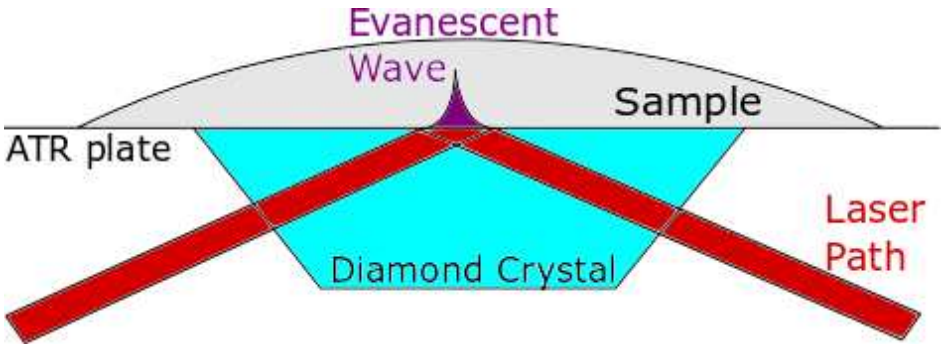

Figure 2.13: Depiction of typical ATR-FTIR measurement process

The ATR-FTIR method is not without its drawbacks. Distortion relative to transmission measurements of the same sample is often introduced due to the interdependence of the real and imaginary components of the refractive index. A sample which strongly absorbs in a certain wavelength range will have a large imaginary component, k, in that range, and possibly zero outside of it. Which also means that the real component, n, will be changing rapidly here as well. As the penetration depth of the evanescent wave depends on this component of the refractive index, the intensity signal that the detector reads is slightly distorted around areas of strong absorption for this reason. Most, if not all, of the current accompanying software to FTIR spectrometers will have an *"ATR correction"* option to correct for this distortion. Another distortion that could be present is when the sample being measured is a homogeneous mixture whose components have different indexes of refraction, but due to the strong absorption of one or more of the components, their indices align causing anomalous dispersion. This behavior has been coined the Christiansen effect [92–94], and is often described as having the same effect as a band pass filter centered at the wavelength at which the indices coincide.

2.5.2 Transmission measurements

Following a similar procedure to that described in 2.4.3, catalyst inks and CCMs were investigated. An initial round of inks with the 0.2 mm spacer were found to be too opaque to get a reliable measurement, so the spacer was replaced with the 0.025 mm spacer and two rounds of measurements were again conducted; one with flowing inks into the cell and flushing with iPa, another with the cell being built and rebuilt around a single drop of the inks. The results of these experiments can be seen in Figure 2.14 and Figure 2.15. This method ultimately offered no clear advantage over ATR. While it was hypothesized that using the nPa spectrum as the reference spectrum would provide adequate results, as nPa is present in relatively large quantities in all samples, this is very evidently not true. The resulting figures showed large spikes in transmission, well above unity, where nPa is known to absorb. Even more qualitative observations are difficult to make, as there does not appear to be any prominent Nafion features present in the inks when comparing them directly to D2020.

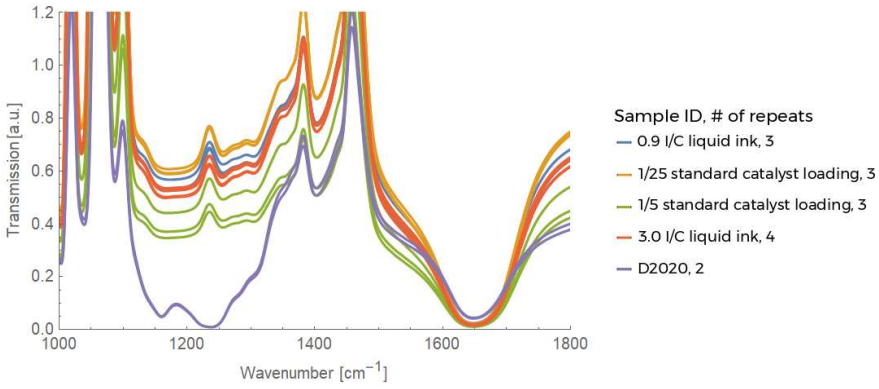

Figure 2.14: IR transmission spectra for various inks using the flow method

Performing the transmission measurements on the CCMs is perhaps more promising, as the spectra seemed to respond strongly to platinum area loading and substrate thickness, (cf, Figure 2.16 & Figure 2.17). Unfortunately, the platinum area loading effect is more likely caused by catalyst layer thickness, as these samples were removed from the spray coating

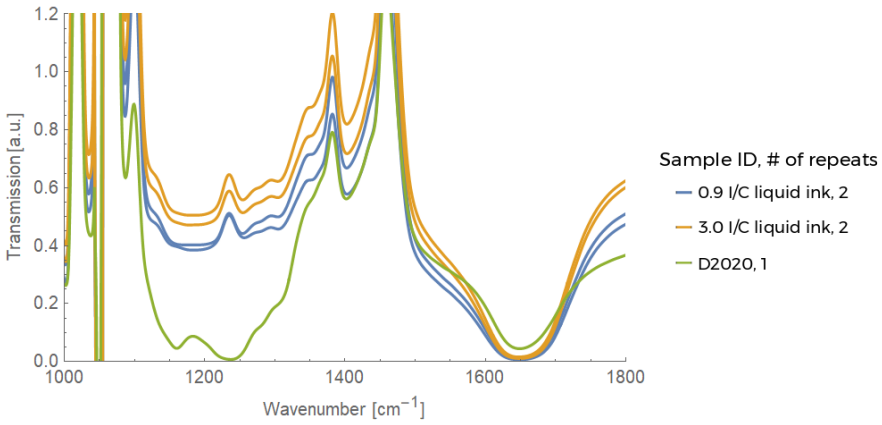

Figure 2.15: IR transmission spectra of ID09IC and ID30IC inks along with D2020 using the single drop method

apparatus prematurely. Meaning that this effect is more likely a scattering effect caused by the different CL thicknesses. It is also difficult to gain any insight into the distribution of ionomer in the CL, or how the signal depends on ionomer content, as the incident light is completely absorbed by the Nafion substrate where we expect to see the two strongest absorption peaks, (the two CF_2 peaks, cf Figure 2.12). Despite these setbacks, it has been shown in literature that the water absorption peaks can be used to determine the hydration of the Nafion membrane [24]. These "peaks" (cf. 3.4.1) are present in all of the CCM transmission data to some degree, meaning that determining the hydration of the underlying membrane is still possible, even after coating.

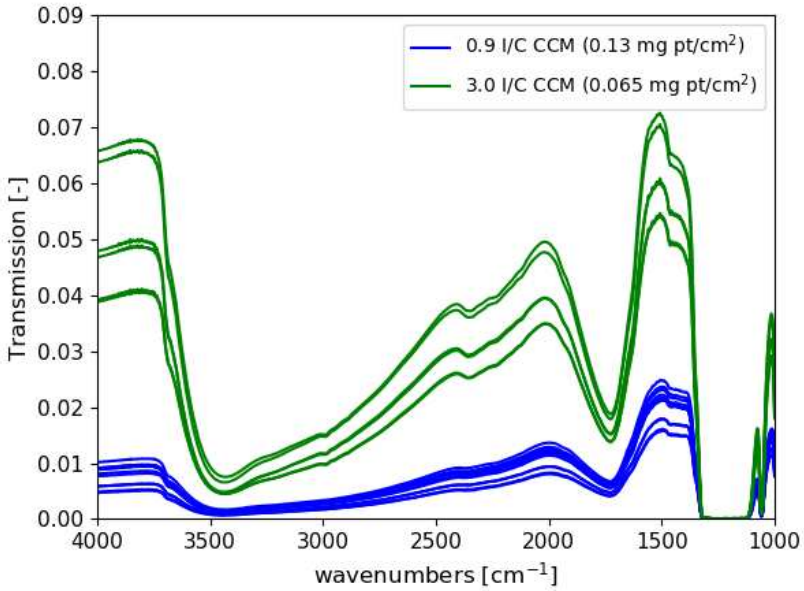

Figure 2.16: IR transmission spectra for CCMs with different platinum loading and ionomer content.

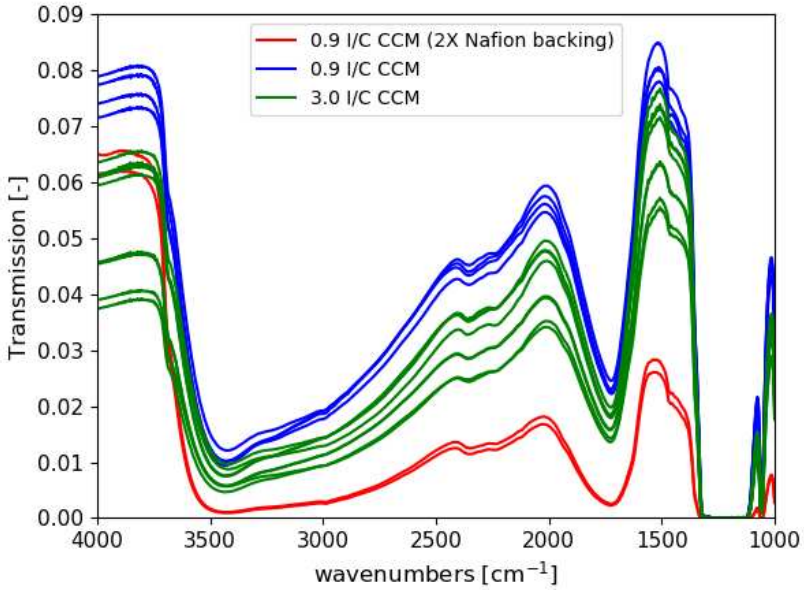

Figure 2.17: IR transmission spectra for CCMs with different ionomer content and support thickness.

CHAPTER 3

ATR-FTIR

3.1 Introduction

As discussed in 2.5.1, attenuated total reflection is a popular method for measuring absorption by taking advantage of the energy in the evanescent wave at the crystal-sample interface. With the failure of the previous methods to detect Nafion features in the catalyst layer, largely due to the the opacity of the inks and the resulting layers, ATR-FTIR seems to be the most promising method as it does not depend on the opacity of the material. Where transmission measurements rely on being able to get light *through* a material, and even more traditional reflection measurements rely on the surface scattering to be small in order to get a strong signal from the specular reflection, ATR-FTIR only requires that the index of refraction of the sample is sufficiently smaller than that of the chosen crystal (recall the condition set by Snell's law, eq.(2.7), θ_c is fixed for ATR attachments limiting how close the indices can match), and that the sample is placed such that it contains the evanescent wave. As light does not penetrate the material in the usual sense, the term "scattering" does not make much sense in this context. The energy in the evanescent wave will be absorbed if the sample absorbs at that wavelength, or it will not. The aberrations discussed earlier may present themselves near where strong absorption takes place, and these will be discussed as they occur.

3.2 Sample preparation

Target ionomer to catalyst (I/C) ratios were chosen about the ideal 0.9 I/C, ranging from 0.5-3.0 I/C. Spray and blade/roll coating ink compositions were considered. Blade/roll coating inks demand a relatively higher viscosity to achieve target layer thickness, whereas spray coating requires a significantly lower viscosity to achieve the flow rates necessary for rapid coating. Individual component masses were calculated, weighed, and mixed in their

respective vials. The mixing method implements two rounds of ten-second horn sonication, (once after de-ionized water is added to the catalyst powder, and again after the addition of the solvent and ionomer); followed by twenty-minutes of ice bath sonication. The catalyst powder was a commercial Vulcan black carbon with 47wt% platinum nanoparticles. The individual masses were converted into approximate volumes by their densities as reported in literature [95–98]. Table 3.1 reports the volumes of the individual components added to the inks as a fraction of the total volume of produced catalyst ink.

Inks with the appropriate spray coating (S) composition were then used to spray several single-sided catalyst coated membranes (CCMs), all with the target platinum loading of 0.1 mg/cm^2; which was later confirmed to be within tolerance by X-ray fluorescence (XRF). These CCMs are reported in Table 3.2, with volume fractions calculated as if the membranes were perfectly dehydrated. The different I/Cs for each method (S and B) were achieved by changing the volume of D2020 (commercial Nafion dispersion produced by Chemours) added to each ink. All other weights were held constant.

Table 3.1: Liquid sample composition for spray coating (S) and blade coating (B)

Sample ID	**Target I/C**	**Composition by volume fraction [%]**				
		Nafion	**Water**	**nPa**	**Carbon**	**Platinum**
D2020	-	6.889	34.680	58.431	-	-
D1021	-	8.200	91.800	-	-	-
S05	0.5	0.036	56.532	43.308	0.115	0.009
S09	0.9	0.064	56.442	43.370	0.114	0.009
S15	1.5	0.106	56.309	43.463	0.113	0.009
S30	3.0	0.208	55.982	43.689	0.112	0.009
B09	0.9	4.347	42.188	52.538	0.859	0.067
B15	1.5	5.476	41.686	51.912	0.859	0.067
B30	3.0	8.298	40.429	50.347	0.859	0.067

3.3 Experimental methods

Absorption spectra was collected using a Nicolet iS50 FTIR spectrometer from Thermo Scientific with 4 cm^{-1} resolution, (0.482 cm^{-1} data spacing), 400-4000 cm^{-1} spectral range,

Table 3.2: Solid spray coated samples and compositions

Sample ID	Sample description	Composition by volume fraction [%]		
		Nafion	Carbon	Platinum
Nafion 211 membrane	-	100	-	-
C09	0.9 I/C CCM	49.2	47.0	3.8
C15	1.5 I/C CCM	61.8	35.4	2.8
C30	3.0 I/C CCM	76.4	21.9	1.7

and 32 scan averaging. A Specac Golden Gate single pass ATR attachment was used to measure all samples (cf. fig. Figure 2.13). Liquid samples were deposited onto the ATR diamond using either the drop or blade-coating method as described below.

3.3.1 Drop method

Spectra were recorded via the drop method using an excess (0.1-0.2 mL) of the samples D2020, D1021, and S05-S30 placed directly on the diamond ATR crystal. After data collection, the surface was wiped clean with iPa and a reference spectra was collected to ensure a properly cleaned surface and negligible variation in baseline absorption. The collection process was repeated for each sample, cycling through the specimens in a randomized order until each had a minimum of three repeated measurements taken. To capture the dynamic characteristics of the catalyst layer formation in situ, the drop-measure-clean cycle was repeated again, while allowing the drops to dry directly on the diamond. Spectra were collected roughly every 90 seconds.

The ATR-FTIR measurement was converted to experimental absorbance by the Beer-Lambert law, rewritten here,

$$a(\nu) = -\ln\left(\frac{I(\nu)}{I_0(\nu)}\right),$$

where $a(\nu)$ is the resulting FTIR absorbance, $I(\nu)$ is the detector signal for the sample being measured, and $I_0(\nu)$ is the average of reference spectra collected in the absence of a sample. No ATR correction was used on the resulting spectra.

3.3.2 Blade coating

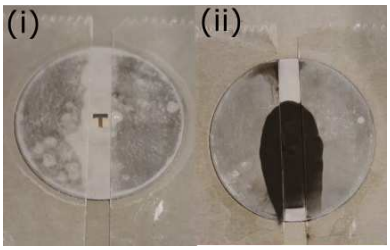

Figure 3.1: Experimental blade coating setup on the ATR plate. (i) Tape on either side of the diamond creating a channel for ink to be coated; (ii) ink droplet properly placed above the upper edge of the diamond.

B-designated samples (B09-B30) were deposited directly onto the ATR diamond using the blade coating technique, (cf, Figure 3.1). This was done by placing two parallel strips of packing tape on either side of the diamond. The inks were deposited along this ≈60 μm deep channel. A 5 μL drop was placed approximately 4 mm above the upper edge of the diamond. A blade, oriented perpendicular to the channel, was then swept down the length, depositing the ink over the diamond. A drying time of <4 minutes was confirmed by the absence of water in the absorbance data. After the ink was dried, three spectra were collected in succession, the diamond surface was cleaned with iPa, and a reference spectra was collected. Nine spectra were collected for each sample in a randomized order.

3.3.3 Catalyst powder spectra

Catalyst powder spectra were collected by drop casting the B-designated samples (B09-30) onto glass slides and allowing them to dry. The resulting dried layers were then scraped onto the ATR diamond, cut into a fine powder, and pressed against the diamond using the anvil attachment. On completion of each measurement, the powder was re-cut and pressed again for three total measurements.

Table 3.3: Significant peak designations

Component	Letter designation	Range [cm^{-1}]	Comment
Nafion	n1	1200	asym. CF_2
Nafion	n2	1150	sym. CF_2
Nafion	n3	900-1100	COC/CF/SO peaks emerging
Water	w1	3400	-
Water	w2	1600	-
nPa	p1	2700-3000	-
nPa	p2	1300-1500	-
nPa	p3	900-1100	-

3.4 Experimental results and discussion

3.4.1 Defining regions of interest and base component contributions

The drop method was used to collect the absorption spectra of the catalyst inks' base components. These components are generally water, n- or iso-propanol (this component will hereafter be interchangeable with the term 'solvent'), and a Nafion dispersion. Figure Figure 3.2 shows the spectra for these components along with a comparison between two Nafion dispersions; one with Nafion dispersed in nPa and water (D2020), and the other dispersed only in water (D1021).

The measured base-component absorption spectra was then used to identify peaks in the mixtures, (cf. Table 3.3). For example, the solvent used in the D2020 Nafion dispersion is easily identified by matching the peaks located between 2700-3000 cm^{-1}, (p1), 1300-1500 cm^{-1}, (p2), and 900-1100 cm^{-1}, (p3). These peaks are absent in the D1021 dispersion, which contains only water. Dispersions which use iPa instead of nPa as a solvent were also tested and found to have a distinct signature in these three outlined regions, (compare p1-3 with p1*-3*), establishing that the composition of the samples is evident from the ATR-FTIR spectra.

It is well established in literature that the two peaks n1 and n2 correspond to symmetric and asymmetric stretching in the CF_2 bonds in the polytetrafluoroethelyne (PTFE) that

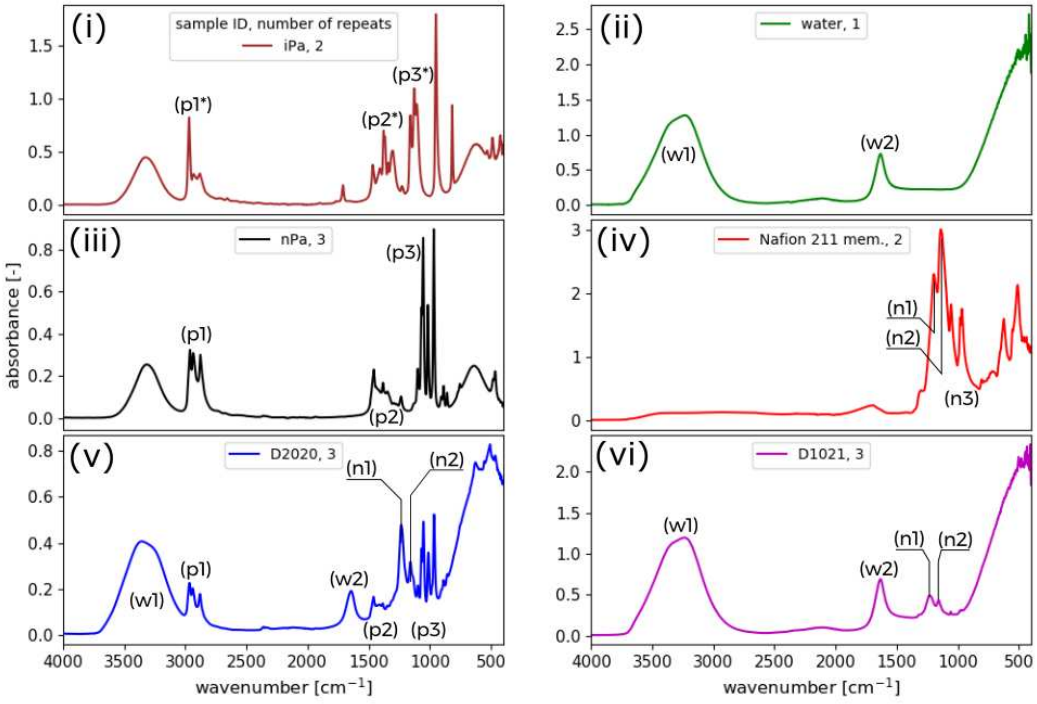

Figure 3.2: Absorbance, $a(\nu)$, spectra for (i) iPa, (ii) water, (iii) nPa, (iv) a Nafion 211 membrane, (v) D2020, and (vi) D1021. Peak designations are used to highlight regions of interest for each of the samples, (cf, Table 3.3).

makes up the Nafion polymer backbone [22, 24, 84]. The water peaks w1 and w2 scale as expected. The D1021, having roughly three times the water as D2020 by volume fraction, shows an absorbance roughly three times greater than that of D2020 at these peak locations. Similarly, nPa makes up a little over half of the D2020 dispersion by volume, and the measured absorbance of the nPa in D2020, in the three regions outlined above, p1, p2, and p3, is roughly half that of pure nPa. It is harder to compare the two Nafion peaks n1 and n2 in D2020 and D1021. The idealized volume fractions of Nafion in the two dispersions have a difference of ≈1% (cf, Table 3.1), however, the n1 and n2 peak shapes of the Nafion membrane and the two dispersions are each slightly different. While the n1 absorption values are roughly equal between D2020 and D1021, as suggested by their near equivalent volumes, the differences in peak shape/width and absorption at n2 may hint at the differences in Nafion's morphology when presented in varying solvents as described in other works [30, 99].

3.4.2 Drop method

Spectra of spray coated inks, (S05-S30), were collected via the drop method (cf, Figure 3.3). All of the specimen repeats for each sample fell on top of each other, typically within a single standard deviation from the mean, for all wavenumbers. The overlapping spectra is expected, as there is a near equivalent volume of both water and nPa in all of the inks (cf, Table 3.1). The two Nafion peaks, n1 and n2, are noticeably absent, as the volumes of Nafion present in each ink is below 0.2%, under the detection limit using ATR-FTIR spectroscopy. This demonstrates the limitations of IR absorption as a quality control check for catalyst inks post-production and immediately prior to spraying. It is possible to take a 0.1 mm drop of a significantly larger batch of ink and use ATR-FTIR spectroscopy to check the relative concentrations of water and solvent, and to confirm that the solvent selected is the correct/intended solvent to be used in the ink. However, the concentrations of Nafion present in these inks are too small to be detectable using single pass ATR-FTIR spectroscopy in liquid form.

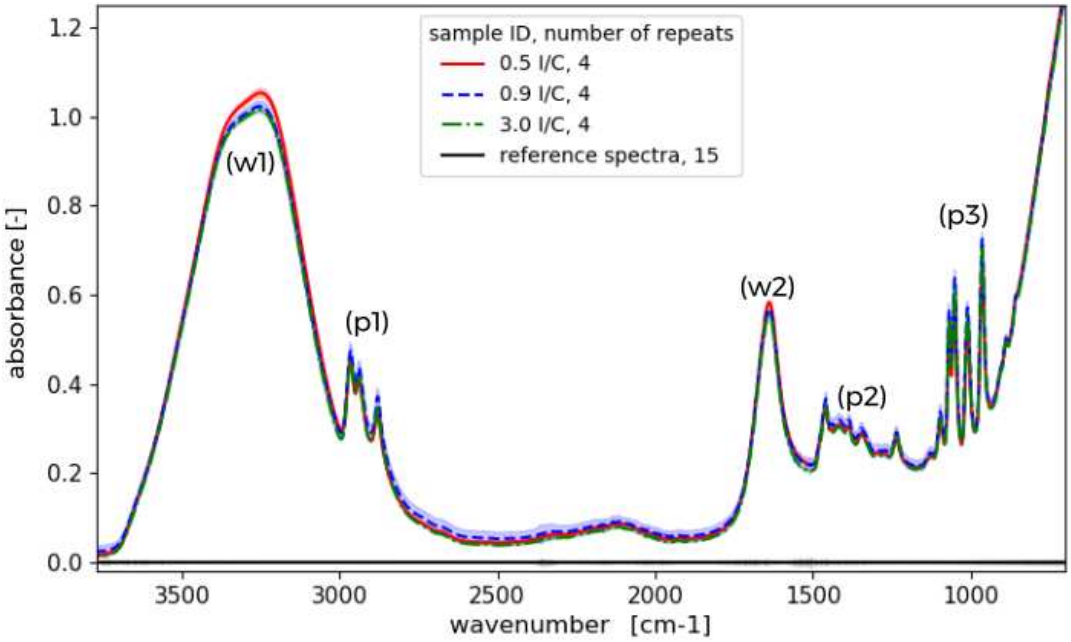

Figure 3.3: Wet ink absorbance spectra; S05-S30 (0.5-3.0 I/C) drop cast in excess (0.1-0.2 mL).

3.4.3 Dynamic catalyst layer formation

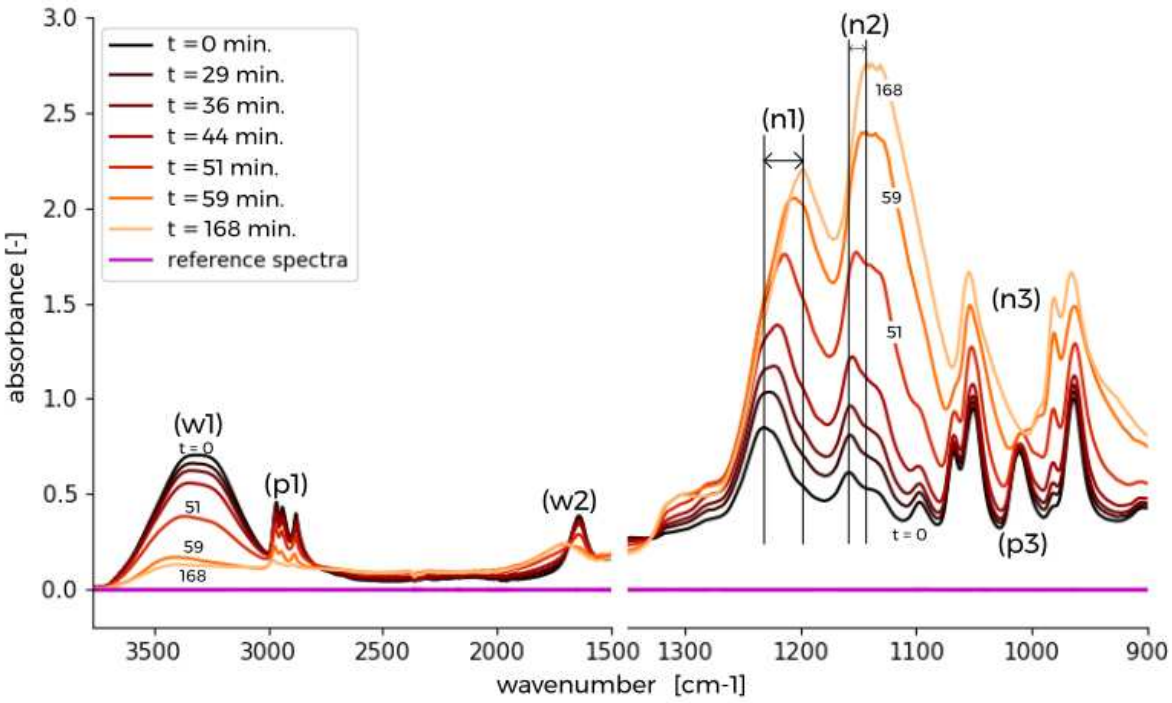

Figure 3.4: Absorbance spectra collected during D2020 drying.

The formation of a Nafion membrane from the D2020 dispersion was recorded in situ, (cf., fig. Figure 3.4), to investigate the dynamic nature of the transition between liquid catalyst ink into a dried solid catalyst layer. This is initially done via the drop casting method, with the darkest line that represents $t = 0$ min., or the first collection; and should match (within relatively small experimental error) with its corresponding spectra in Figure 3.2v. The rapid evaporation of both the nPa (p1-p3) and the water (w1-w2) is represented by the decrease in absorbance between time steps. The process primarily occurs between the 28^{th} and 58^{th} minutes. As the water and solvent evaporate the volume fraction of Nafion increases, (absorbance of the CF_2 peaks, n1 and n2, nearly triples). Peaks affiliated with Nafion's sulfonic acid side chain also emerge; such as the COC/CF and SO peaks at 900 and 1100 cm^{-1} (n3) respectively [15, 84, 90], which were previously obscured by the water and solvent absorption (this is shown even more clearly in fig. Figure 3.5). The two CF_2 peaks

n1 and n2 shift towards lower wavenumbers: from 1230 and 1157 cm^{-1} to 1200 and 1136 cm^{-1} respectively, which is much closer to the values reported in literature for solid Nafion membranes [84]. It is then hypothesized that the absorption peak intensity is a measure of the relative concentration of the Nafion molecule, while the peak location is a measure of its polymerization.

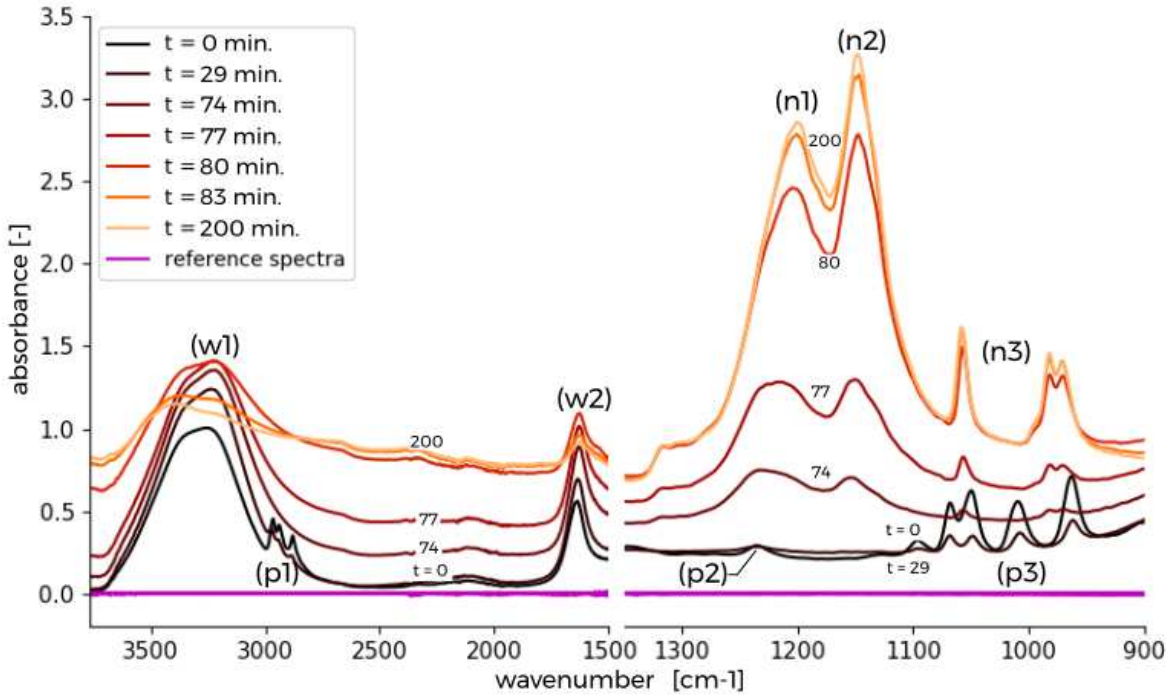

Figure 3.5: Absorbance spectra collected during 3.0 I/C ink (S30) drying

Repeating this process of drop casting S-designated inks and taking measurements as the droplets dried by natural convection produced an array of figures, with Figure 3.5 being the most notable. As shown, the absorbance measured during the ink drying exhibits similar behavior except for an additional vertical baseline shift which generally increases as the sample dries. This vertical baseline shift is believed to be caused by the index of refraction matching between the diamond crystal in the ATR plate and the carbon black powder in the sample. As the water and solvent evaporate the index of refraction of the catalyst film approaches that of the diamond, decreasing the reflection at the diamond/catalyst film

interface. Focusing on regions p1 and p2 the real time evaporation of nPa is clearly visible. Region p3 highlights the transition from nPa, p3, to Nafion, n3, peaks, which are part of the Nafion side chains and were previously below the detection limit. While previous measurements on these inks in liquid form failed to detect any amount of Nafion, Nafion is detectable after evaporating the solvent and some of the water away. The repeatability of these measurements suffers significantly from settling effects present in the films, (described in Section 3.4.4), thus necessitating a new deposition method.

3.4.4 Nonuniform drying behavior of catalyst inks

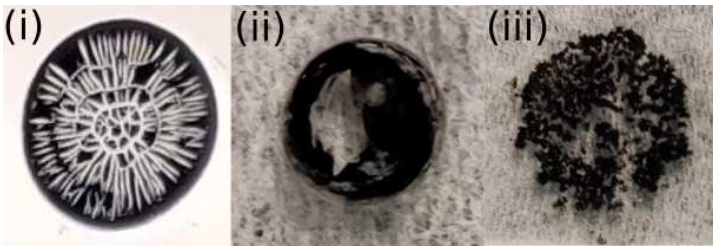

Figure 3.6: Three types of complications observed when drying inks onto substrates. (i) shows B09, (which had a higher viscosity) dried directly onto a glass slide substrate. (ii) shows S09 dried onto a Nafion substrate (made by drying a drop of similar size of D2020 onto the glass substrate). (iii) shows S09 again, dried directly onto a glass substrate.

Unfortunately, when the inks were deposited by drop casting onto the ATR plate, they exhibited a combination of three types of nonuniform drying behavior, which made quantitative analysis difficult. Figure 3.6 illustrates the three common drying behaviors observed after drop casting the catalyst inks. These can be characterized as cracking (Figure 3.6i), coffee ring effect (Figure 3.6ii), and agglomerating catalyst support particles falling out of suspension (Figure 3.6iii). When an S-designated ink was placed on the ATR plate, agglomerations immediately began to form and fall out of suspension, leading to a drying pattern similar to Figure 3.6iii over the diamond. This led to highly variable Nafion absorption measurements at peaks n1 and n2; and inconsistent baseline shifting. Experimenting with different substrates led to depositing S-designated inks onto a thin Nafion film, (cf, Fig-

ure 3.6ii), resulting in the ink beading up. The drying behavior of suspended particles in beads produced the well known coffee ring effect, as depicted. The more viscous B-designated inks were also dried on glass slides to see if they exhibited similar behavior. The additional viscosity was beneficial in that these inks beaded without the need to change substrates. However, they exhibited cracking (Figure 3.6i), which is common for blade coatings which exceed the maximum single pass layer thickness [100–104]. Due to the persistent nature of these effects despite several iterative changes to the drying procedure, and the unpredictable experimental error introduced by the drying patterns, it was determined that the drop method is not appropriate for quantitative analysis.

3.4.5 Blade coating

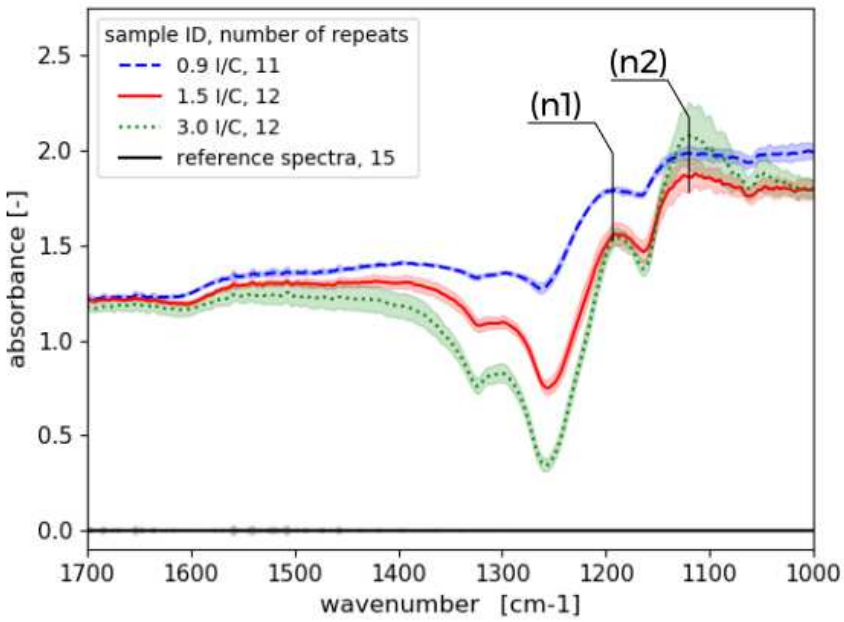

Figure 3.7: Normalized absorbance spectra for catalyst layer formation after blade coating B09-B30 and baseline shift correction. Each line represents the spectra averaged over all of the repeated measurements for that sample. The shaded area around them represents plus/minus one standard deviation from this mean.

Catalyst films were prepared using B-designated inks and the aforementioned blade coating method. From the initial absorbance data, there was no apparent correlation between losses from index of refraction matching between the diamond and catalyst thin film, (presenting as baseline shifting), and the ionomer loading. As this baseline shifting is detrimental to quantitatively comparing absorbance spectra between samples, each spectrum was normalized to its absorption at 2500 cm^{-1}. Performing the normalization produced Figure 3.7. This process proved to be highly consistent in its deposition quality (determined visually), and its repeatability in producing consistent spectra.

Increasing I/C corresponded to a decrease in the measured absorbance between 1100-1500 cm^{-1}. The separation between spectra is statistically significant as the shading around each line represents +/- one standard deviation. With the problems of repeatability of absorbance measurements, inconsistent interface losses, and visual nonuniformity problems all solved, ATR-FTIR appears to be a promising method for ionomer characterization in catalyst inks.

3.4.6 Catalyst powder spectra

To further investigate the observed drops in absorption, the dried catalyst films were ground into a powder and the spectra was collected again to ensure similar measurements can be taken without directly coating the ATR plate. After performing the same baseline normalization, Figure 3.8 was produced, confirming the results of the previous experiment. The spectra have again separated themselves out by decreasing I/C in the previously defined region of interest. However, a feature that is not shared is the region of the 3.0 I/C spectra below ≈1200 wavenumbers, where the absorbance jumps up above the others. This jump in absorbance is likely due to the lack of infrared light making it to the detector at these wavenumbers, due to the increased loss present in these samples from index matching. This is seen in the raw spectra, not presented here.

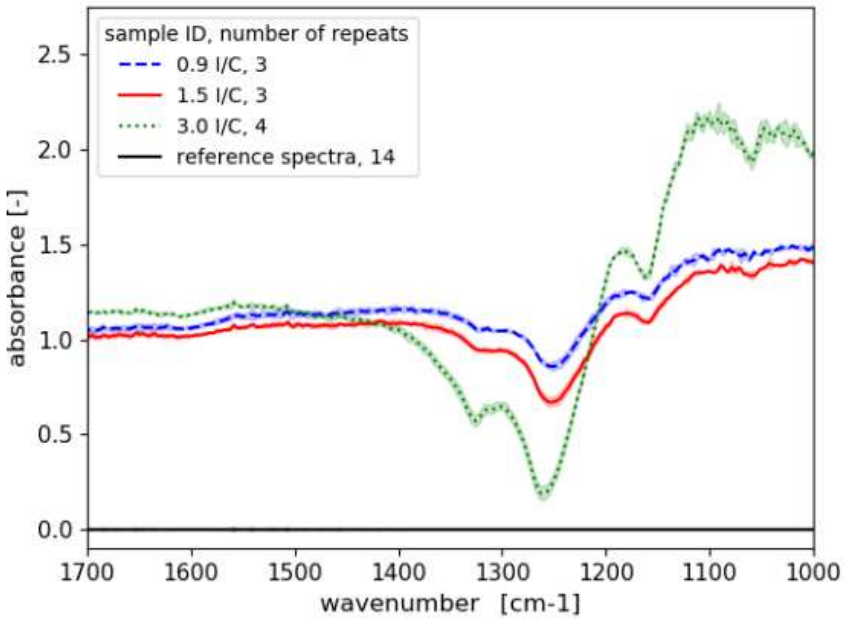

Figure 3.8: Normalized absorbance spectra for catalyst powder (B09-B30 dried) crushed against ATR diamond with anvil

3.4.7 Dynamic catalyst layer formation with anomalous dispersion

The transition from the absorption to anomalous dispersion can be observed in real time by recording spectra as the samples dry on the diamond, similar to the previous catalyst thin film formation measurements.

Similar to Figure 3.4 and Figure 3.5, Figure 3.9 shows Nafion peaks (n1 and n2) emerging from the solvent/water dominated initial spectrum. As the solvent evaporates, the anomalous dispersion feature begins to form, even while there is still water present. The final dried spectrum then shows the absorption response dominated largely by the index matching of the mixture and the diamond, punctuated by the dip in absorption caused by the anomalous dispersion of the Nafion.

The dips in absorption corresponding to increasing I/C in the B-designated samples can be attributed to anomalous dispersion caused by the large changes in the real index of refraction near strong absorption peaks. Near where the Nafion strongly absorbs (the CF_2

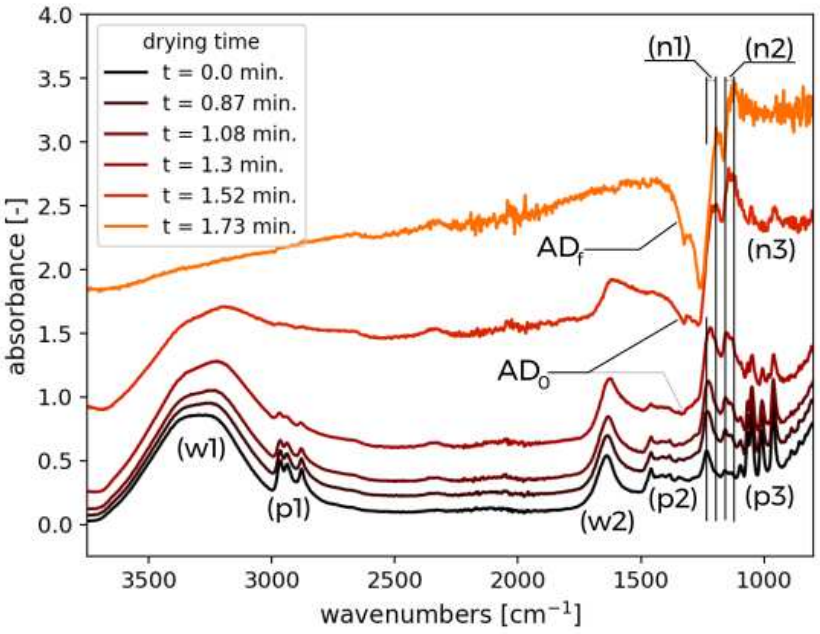

Figure 3.9: 3.0 I/C (B30) ink drying after blade coating. The recording interval between the start of each spectra collection was set to approximately 13 seconds. Peak designations have been marked as with previous drying figures. The initial emergence of anomalous dispersion (AD_0) feature is marked along with the fully formed feature (AD_f).

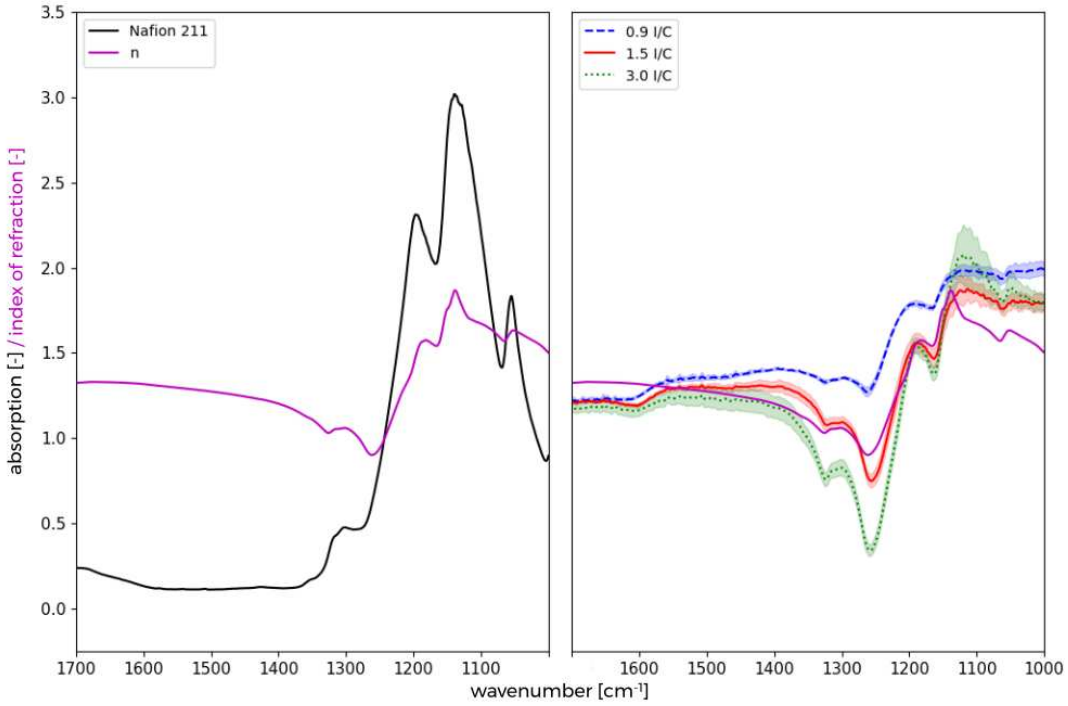

Figure 3.10: Real component of the index of refraction of Nafion overlain on the absorption spectrum of the Nafion 211 membrane (left) and the spectrum collected during the blade coating experiment (right).

peaks n1 and n2), the difference in indices between the individual catalyst film components and the diamond rapidly fluctuates and causes the observed decrease in absorption of the blade coated spectra. This phenomena is described as the Christiansen effect, and is further described elsewhere [92–94]. The experimental absorption spectrum of the Nafion 211 membrane was fed into a commercial software (*EssentialFTIR*) which returned n and k over the absorption spectrum. This is shown in Figure 3.10.

3.5 Computing I/C from anomalous dispersion

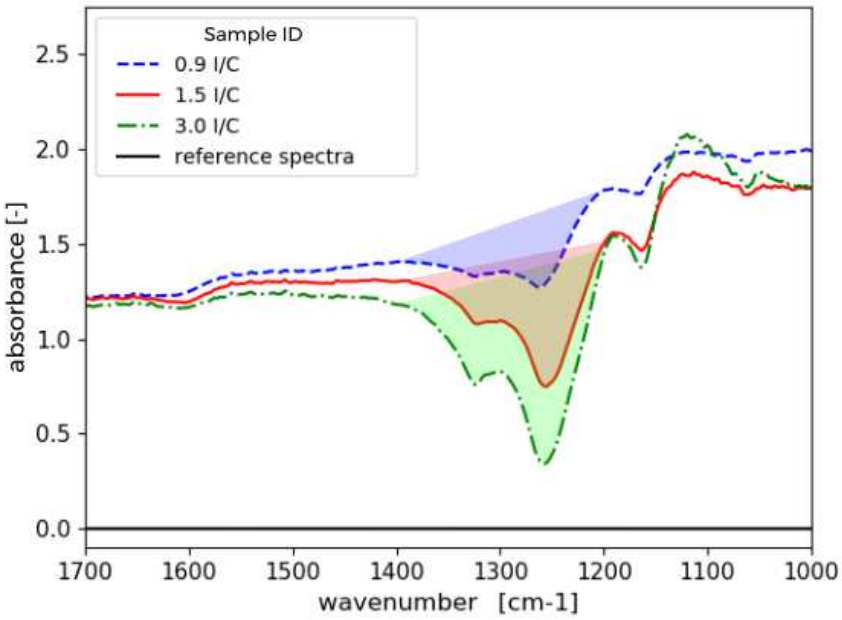

Figure 3.11: Illustration of area calculation using numerical integration, (1400-1200 cm^{-1}).

To further quantify the responses from blade coating (Figure 3.7) and the powdered catalyst (Figure 3.8), the area partially bounded by these curves and a line segment enclosing them were calculated; along with their lowest points. The spectral range for integration was chosen to be 1200-1400 cm^{-1} as this range sufficiently encapsulates the response. A line segment was drawn for each absorbance measurement between the bounds to define the upper bound of the area of integration. This is depicted in Figure 3.11 showing the enclosed area

as the shaded regions between 1200 and 1400 wavenumbers. The area was then calculated using a left Riemann sum numerical integration method on the vertical distance between the line segment and the absorbance, with a step size in wavenumbers, δ, matched to the data spacing of the spectrometer, 0.48 cm^{-1}. This area is reported in Figure 3.12.

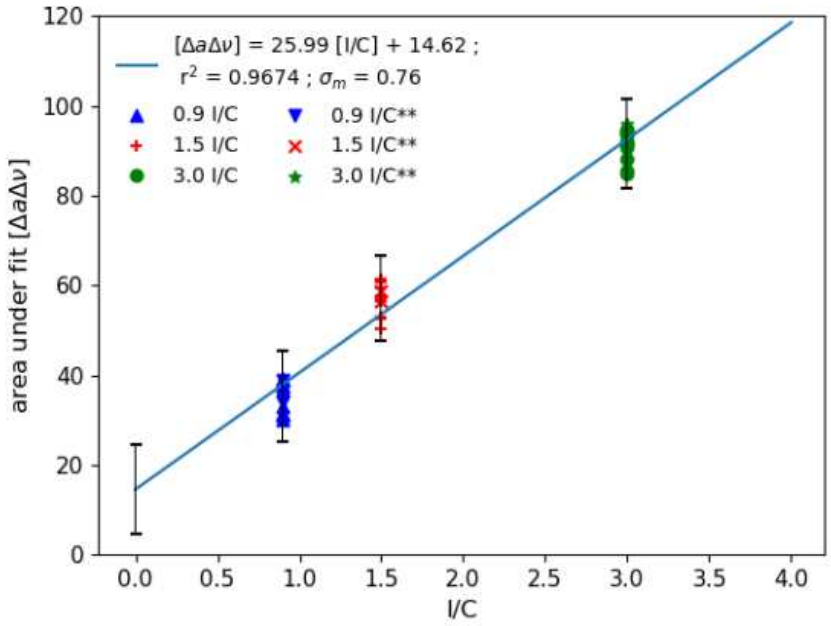

Figure 3.12: Calculated absorbance area for blade coating spectra by I/C using a left Riemann sum, (*n = 11-12*); dataset includes a trend line for extrapolating the data. ** data points are the final spectra from the in situ drying study (cf. fig Figure 3.9, *n = 2*). Black error bars represent $\pm 3\sigma$ from the mean with the error at I/C = 0 being $\pm 3\times$ the average standard deviation of the three sets from the extrapolated zero point.

3.6 Conclusions

ATR-FTIR was found to be successful in several different aspects of catalyst ink and thin film characterization which could be useful in the implementation of quality control measures. From the inks pre CCM production, relative concentrations of water and solvent can be evaluated. By allowing as little as 5 μL of ink to dry, it is possible to measure dynamic drying behavior, such as the evaporation times of the water and solvent, and the relative level of ionomer polymerization via peak shifting. It was shown that the ionomer content

of the dried catalyst films correspond to sharp dips in absorption following the real index of refraction of Nafion. This dip in absorption is caused by anomalous dispersion due to the strong absorption bands of Nafion immediately adjacent to the dips. After normalization, the separation between spectra of inks with differing I/C was found to be statistically significant ($> 3\sigma$) in the above defined region of interest. In calculating the area defined by the deviation of the absorption here from a line segment bounding the dips, a trend line was calculated which may be used in extrapolating films with different I/C's than those tested. This area calculation requires no normalization as the baseline shifting does not noticeably effect the area bounded by the anomalous response.

CHAPTER 4
CONCLUSIONS AND FUTURE WORK

In order to meet the growing demand for fuel cells, several methodologies have been tested here in order to determine their effectiveness in measuring ionomer concentration in the catalyst layer; something that is both essential to fuel cell operation, and effectively absent in quality control measures. Raman spectroscopy has been used elsewhere in the mapping of PTFE in a carbon fiber support, but has been deemed unsuitable for the purposes of inline quality control as the method does not scale particularly well and has been shown to be destructive when used on CCMs. Capacitive imaging, a popular NDE in industrial settings, was briefly investigated by ideally modeling a capacitive system and was found to be more sensitive to deviations in substrate thickness than to the loading of the ionomer in the catalyst layer. UV-visible and FTIR transmission measurements were taken, the former spectra being essentially unusable due to the opaque nature of the samples, and the latter giving little insight into the nature of ionomer in the catalyst layer as the substrate absorbed the IR light in the spectral range of interest completely.

ATR-FTIR proved to be a more promising method. It is shown here that the solvents used in Nafion dispersions are able to be positively identified in minutes using the absorption markers defined previously, which eliminates the concern of using mislabeled dispersions of the wrong solvent or even dispersions in which Nafion is absent. Similarly, relative quantities of solvent (nPa/iPa) and water in catalyst inks can be determined using this method, however, the concentration of Nafion is below the detection limit for this single pass method. Furthermore, it is possible to see the level of polymerization in real time during the formation of a Nafion membrane by measuring the shifting of the CF_2 peaks during the drying process. Finally, it was shown that by taking advantage of the area of anomalous dispersion present in the catalyst layer from the strong CF_2 absorption, it is possible to order samples by their

ionomer to catalyst ratio with high accuracy, ($> 3\sigma$); which no previously reported method has been shown to be capable of doing.

Further work includes expanding the ATR test matrix in order to work out a definitive equation to be used in calculating the I/C ratio in the CL. The present work offers a line of best fit to perform this approximation, however, with only a single batch of each ink to draw from, variation in batches with the same target I/C has yet to be tested. Subsequent work is then to translate the findings of this study into a methodology suitable for inline quality control purposes. As the ATR method is not amenable to high throughput inline measurements, this task is indeed quite daunting. Yet, diffuse reflection off of the CCM may provide surface level deposition information similar to the results provided here, though, the signal intensity of the diffuse light is again in question. Further experimentation is required to answer this.

REFERENCES CITED

[1] IPCC, 2018: Summary for Policymakers. In: *Global Warming of 1.5°C. An IPCC Special Report on the impacts of global warming of 1.5 °C above pre-industrial levels and related global greenhouse gas emission pathways, in the context of strengthening the global response to the threat of climate change, sustainable development, and efforts to eradicate poverty* [Masson-Delmotte, V., P. Zhai, H.-O. Pörtner, D. Roberts, J. Skea, P.R. Shukla, A. Pirani, W. Moufouma-Okia, C. Péan, R. Pidcock, S. Connors, J.B.R. Matthews, Y. Chen, X. Zhou, M.I. Gomis, E. Lonnoy, T. Maycock, M. Tignor, and T. Waterfield (eds.)]. *World Meteorological Organization, Geneva, Switzerland, 32 pp.*

[2] P. D. A. Kraaijenbrink, M. F. P. Bierkens, A. F. Lutz, and W. W. Immerzeel, "Impact of a global temperature rise of 1.5 degrees Celsius on Asia's glaciers," Nature, vol. 549, pp. 257–260, Sept. 2017.

[3] M. Vermeer and S. Rahmstorf, "Global sea level linked to global temperature," Proceedings of the National Academy of Sciences, vol. 106, no. 51, pp. 21527–21532, 2009. Publisher: National Academy of Sciences _eprint: https://www.pnas.org/content/106/51/21527.full.pdf.

[4] J. M. Mitchell, A Preliminary Evaluation of Atmospheric Pollution as a Cause of the Global Temperature Fluctuation of the Past Century, pp. 139–155. Dordrecht: Springer Netherlands, 1970.

[5] "Toyota moves to expand mass-production of fuel cell stacks and hydrogen tanks towards ten-fold increase post-2020." `https://newsroom.toyota.co.jp/en/corporate/22647198.html`. Toyota Motor Corporation, accessed: 2018-10-18.

[6] M. Watanabe, H. Igarashi, and K. Yosioka, "An experimental prediction of the preparation condition of Nafion-coated catalyst layers for PEFCs," Electrochimica Acta, vol. 40, pp. 329–334, Feb. 1995.

[7] Y. Ayato, K. Kunimatsu, M. Osawa, and T. Okada, "Study of pt electrode/nafion ionomer interface in $HClO_4$ by in situ surface-enhanced FTIR spectroscopy," Journal of The Electrochemical Society, vol. 153, no. 2, p. A203, 2006.

[8] K. Kanamura, H. Morikawa, and T. Umegaki, "Observation of interface between pt electrode and nafion membrane," Journal of The Electrochemical Society, vol. 150, no. 2, p. A193, 2003.

[9] K. Kunimatsu, M. Samant, H. Seki, and M. Philpott, "Study of HSO4 and SO4 co-adsorption on a platinum electrode in H2SO4 by in-situ FTIR," J. Electroanal. Chem., vol. 243, pp. 203–208, 1988.

[10] K. Kunimatsu, M. Samant, and H. Seki, "In situ FTIR spectroscopic study of bisulfate and sulfate adsorption on platinum electrodes," J. Electroanal. Chem., vol. 258, pp. 163–177, 1989.

[11] K. Kunimatsu, T. Yoda, D. A. Tryk, H. Uchida, and M. Watanabe, "In situ atr-ftir study of oxygen reduction at the pt/nafion interface," Phys. Chem. Chem. Phys., vol. 12, pp. 621–629, 2010.

[12] A. Miki, S. Ye, and M. Osawa, "Surface-enhanced ir absorption on platinum nanoparticles: an application to real-time monitoring of electrocatalytic reactions," Chem. Commun., pp. 1500–1501, 2002.

[13] I. Yagi, K. Nomura, H. Notsu, K. Kimijima, and N. Ohta, "In situ observation of nafion-model molecular behaviors at metal electrodes by SEIRAS," 2011.

[14] J. Zeng, D.-i. Jean, C. Ji, and S. Zou, "In Situ Surface-Enhanced Raman Spectroscopic Studies of Nafion Adsorption on Au and Pt Electrodes," Langmuir, vol. 28, pp. 957–964, Jan. 2012.

[15] Z. Liang, W. Chen, J. Liu, S. Wang, Z. Zhou, W. Li, G. Sun, and Q. Xin, "FT-IR study of the microstructure of Nafion membrane," Journal of Membrane Science, vol. 233, pp. 39–44, Apr. 2004.

[16] K. Malek, M. Eikerling, Q. Wang, T. Navessin, and Z. Liu, "Self-Organization in Catalyst Layers of Polymer Electrolyte Fuel Cells," The Journal of Physical Chemistry C, vol. 111, pp. 13627–13634, Sept. 2007.

[17] K. Malek, T. Mashio, and M. Eikerling, "Microstructure of Catalyst Layers in PEM Fuel Cells Redefined: A Computational Approach," Electrocatalysis, vol. 2, pp. 141–157, June 2011.

[18] K. A. Mauritz and R. B. Moore, "State of Understanding of Nafion," Chemical Reviews, vol. 104, pp. 4535–4586, Oct. 2004.

[19] T. D. Gierke, G. E. Munn, and F. C. Wilson, "The morphology in nafion perfluorinated membrane products, as determined by wide- and small-angle x-ray studies," Journal of Polymer Science: Polymer Physics Edition, vol. 19, pp. 1687–1704, Nov. 1981.

[20] E. Moukheiber, G. De Moor, L. Flandin, and C. Bas, "Investigation of ionomer structure through its dependence on ion exchange capacity (IEC)," Journal of Membrane Science, vol. 389, pp. 294–304, Feb. 2012.

[21] T. Suzuki, S. Tsushima, and S. Hirai, "Effects of Nafion ionomer and carbon particles on structure formation in a proton-exchange membrane fuel cell catalyst layer fabricated by the decal-transfer method," Hydrogen Energy, p. 9, 2011.

[22] A. Gruger, A. Régis, T. Schmatko, and P. Colomban, "Nanostructure of Nafion membranes at different states of hydration: An IR and Raman study," Vibrational Spectroscopy, vol. 26, pp. 215–225, Nov. 2001.

[23] Z. Lu, G. Polizos, D. D. Macdonald, and E. Manias, "State of water in perfluorosulfonic ionomer (nafion 117) proton exchange membranes," Journal of The Electrochemical Society, vol. 155, no. 2, p. B163, 2008.

[24] M. Ludvigsson, J. Lindgren, and J. Tegenfeldt, "Ftir study of water in cast nafion films," Electrochimica Acta - ELECTROCHIM ACTA, vol. 45, pp. 2267–2271, 03 2000.

[25] V. Kozlov, N. Bunkin, I. PS, A. Shkirin, S. Zakharov, and Z. AA, "Study of the phase states of water close to nafion interface," Water, vol. 4, pp. 129 – 154, 03 2013.

[26] Y. P. Patil, T. A. P. Seery, M. T. Shaw, and R. S. Parnas, "In Situ Water Sensing in a Nafion Membrane by Fluorescence Spectroscopy," Industrial & Engineering Chemistry Research, vol. 44, pp. 6141–6147, Aug. 2005.

[27] Y. Tabuchi, R. Ito, S. Tsushima, and S. Hirai, "Analysis of in situ water transport in Nafion by confocal micro-Raman spectroscopy," Journal of Power Sources, vol. 196, pp. 652–658, Jan. 2011.

[28] G. Xie and T. Okada, "FTIR spectroscopy study of fully hydrated nafion membranes," Zeitschrift fur physikalische chemie, vol. 205, pp. 113–125, 1998.

[29] T. A. Zawodzinski, C. Derouin, S. Radzinski, R. Sherman, V. T. Smith, and T. E. Springer, "Water Uptake by and TransportThrough Nafion 117 Membranes," J. Electrochem. Soc., vol. 140, no. 4, p. 7, 1993.

[30] S.-J. Lee, T. Yu, H.-L. Lin, W.-H. Liu, and C.-L. Lai, "Solution properties of nafion in methanol/water mixture solvent," Polymer, vol. 45, no. 8, pp. 2853 – 2862, 2004.

[31] P. A. Cirkel and T. Okada, "A comparison of mechanical and electrical percolation during the gelling of nafion solutions," Macromolecules, vol. 33, no. 13, pp. 4921–4925, 2000.

[32] S. A. Mauger, K. C. Neyerlin, A. C. Yang-Neyerlin, K. L. More, and M. Ulsh, "Gravure Coating for Roll-to-Roll Manufacturing of Proton-Exchange-Membrane Fuel Cell Catalyst Layers," Journal of The Electrochemical Society, vol. 165, pp. F1012–F1018, Jan. 2018.

[33] P. Rupnowski, M. Ulsh, B. Sopori, B. G. Green, D. L. Wood, J. Li, and Y. Sheng, "In-line monitoring of Li-ion battery electrode porosity and areal loading using active thermal scanning - modeling and initial experiment," Journal of Power Sources, vol. 375, pp. 138–148, Jan. 2018.

[34] M. Ulsh, A. DeBari, J. M. Berliner, I. V. Zenyuk, P. Rupnowski, L. Matvichuk, A. Z. Weber, and G. Bender, ""The development of a through-plane reactive excitation technique for detection of pinholes in membrane-containing MEA sub-assemblies"," International Journal of Hydrogen Energy, vol. 44, pp. 8533–8547, Mar. 2019.

[35] High Throughput and High Resolution In-Line Monitoring of PEMFC Materials by Means of Visible Light Diffuse Reflectance Imaging and Computer Vision, vol. ASME 2015 13th International Conference on Fuel Cell Science, Engineering and Technology of International Conference on Fuel Cell Science, Engineering and Technology, 06 2015.

[36] P. Rupnowski and M. J. Ulsh, "Thickness mapping using multispectral imaging," 11 2019.

[37] S. Shukla, K. Domican, K. Karan, S. Bhattacharjee, and M. Secanell, "Analysis of Low Platinum Loading Thin Polymer Electrolyte Fuel Cell Electrodes Prepared by Inkjet Printing," Electrochimica Acta, vol. 156, pp. 289–300, Feb. 2015.

[38] A. Kriston, T. Xie, D. Gamliel, P. Ganesan, and B. N. Popov, "Effect of ultra-low Pt loading on mass activity of polymer electrolyte membrane fuel cells," Journal of Power Sources, vol. 243, pp. 958–963, Dec. 2013.

[39] N. V. Aieta, P. K. Das, A. Perdue, G. Bender, A. M. Herring, A. Z. Weber, and M. J. Ulsh, "Applying infrared thermography as a quality-control tool for the rapid detection of polymer-electrolyte-membrane-fuel-cell catalyst-layer-thickness variations," Journal of Power Sources, vol. 211, pp. 4–11, Aug. 2012.

[40] A. J. Mendoza, M. A. Hickner, J. Morgan, K. Rutter, and C. Legzdins, "Raman spectroscopic mapping of the carbon and ptfe distribution in gas diffusion layers," Fuel Cells, vol. 11, no. 2, pp. 248–254, 2011.

[41] A. Mendoza, C. Legzdins, and M. Hickner, "Chemical mapping of gas diffusion layers," in American Chemical Society - 238th National Meeting and Exposition, ACS 2009, Abstracts of Scientific Papers, 2009. 238th National Meeting and Exposition of the American Chemical Society, ACS 2009 ; Conference date: 16-08-2009 Through 20-08-2009.

[42] T. Böhm, R. Moroni, M. Breitwieser, S. Thiele, and S. Vierrath, "Spatially Resolved Quantification of Ionomer Degradation in Fuel Cells by Confocal Raman Microscopy," Journal of The Electrochemical Society, vol. 166, pp. F3044–F3051, Jan. 2019.

[43] M. Hara, "Electrochemical and Raman Spectroscopic Evaluation of Pt/Graphitized Carbon Black Catalyst Durability for the Start/Stop Operating Condition of Polymer Electrolyte Fuel Cells," p. 55.

[44] T. Jawhari, A. Roid, J. Casado, S. Cientifico-Tkcnics, de Barcelona, I. de Citncia, de Materials, de Barcelona, de Investigacibn, and S. E. de Carburos, "RAMAN SPECTROSCOPIC CHARACTERIZATION OF SOME COMMERCIALLY AVAILABLE CARBON BLACK MATERIALS," p. 5.

[45] A. C. Ferrari, J. C. Meyer, V. Scardaci, C. Casiraghi, M. Lazzeri, F. Mauri, S. Piscanec, D. Jiang, K. S. Novoselov, S. Roth, and A. K. Geim, "Raman Spectrum of Graphene and Graphene Layers," Physical Review Letters, vol. 97, p. 187401, Oct. 2006.

[46] A. C. Ferrari, "Raman spectroscopy of graphene and graphite: Disorder, electron–phonon coupling, doping and nonadiabatic effects," Solid State Communications, p. 11, 2007.

[47] A. C. Ferrari, "Raman spectroscopy as a versatile tool for studying the properties of graphene," NATURE NANOTECHNOLOGY, vol. 8, p. 12, 2013.

[48] I. Kendrick, J. Fore, J. Doan, N. Loupe, A. Vong, N. Dimakis, M. Diem, and E. S. Smotkin, "Operando Raman Micro-Spectroscopy of Polymer Electrolyte Fuel Cells," Journal of The Electrochemical Society, p. 8, 2016.

[49] G. Diamond, D. A. Hutchins, K. K. Leong, and T. H. Gan, "Electrostatic Capacitive Imaging: A New NDE Technique," AIP Conference Proceedings, vol. 894, pp. 689–694, Mar. 2007.

[50] X. Yin, G. G. Diamond, and D. A. Hutchins, "Further investigations into capacitive imaging for NDE," vol. 51, no. 9, p. 8, 2009.

[51] X. Yin, "Non-destructive evaluation of concrete using a capacitive imaging technique: Preliminary modelling and experiments," Cement and Concrete Research, p. 10, 2010.

[52] X. Yin and D. A. Hutchins, "Non-destructive evaluation of composite materials using a capacitive imaging technique," Composites Part B: Engineering, vol. 43, pp. 1282–1292, Apr. 2012.

[53] S. Gupta and K. J. Loh, "A planar array capacitive imaging system for detecting damage in composite structures: a numerical study," p. 11.

[54] X. Yin, G. Chen, W. Li, and D. A. Huthchins, "Design and characterization of planar capacitive imaging probe based on the measurement sensitivity distribution," AIP Conference Proceedings, vol. 1511, pp. 1586–1592, Jan. 2013.

[55] X. Yin, D. A. Hutchins, G. Chen, and W. Li, "Investigations into the measurement sensitivity distribution of coplanar capacitive imaging probes," NDT & E International, vol. 58, pp. 1–9, Sept. 2013.

[56] M. Morozov, W. Jackson, and S. G. Pierce, "Capacitive imaging of impact damage in composite material," Composites Part B: Engineering, vol. 113, pp. 65–71, Mar. 2017.

[57] C. Li, X. Yin, Z. Li, W. Li, and G. Chen, "Positive and negative variations in capacitive images for given defects under varying experimental conditions," p. 6.

[58] Z. Liu and H. Liu, "Experimenting capacitive sensing technique for structural integrity assessment," in 2017 IEEE International Conference on Industrial Technology (ICIT), pp. 922–927, Mar. 2017.

[59] X. Yin, D. A. Hutchins, G. Chen, W. Li, and Z. Xu, "Studies of the factors influencing the imaging performance of the capacitive imaging technique," NDT & E International, vol. 60, pp. 1–10, Dec. 2013.

[60] X. Yin, C. Li, Z. Li, W. Li, and G. Chen, "Lift-off Effect for Capacitive Imaging Sensors," Sensors, vol. 18, p. 4286, Dec. 2018.

[61] X. Yin, Z. Li, A. Yan, W. Li, G. Chen, and D. A. Hutchins, "Further capacitive imaging experiments using modified probes," AIP Conference Proceedings, vol. 1706, p. 090013, Feb. 2016.

[62] Y. Song, H. Xu, Y. Wei, H. R. Kunz, L. J. Bonville, and J. M. Fenton, "Dependence of high-temperature PEM fuel cell performance on Nafion® content," Journal of Power Sources, vol. 154, pp. 138–144, Mar. 2006.

[63] F. Lufrano, P. Staiti, and M. Minutoli, "Influence of Nafion Content in Electrodes on Performance of Carbon Supercapacitors," Journal of The Electrochemical Society, vol. 151, pp. A64–A68, Jan. 2004.

[64] E. Antolini, L. Giorgi, A. Pozio, and E. Passalacqua, "Influence of Nafion loading in the catalyst layer of gas-diffusion electrodes for PEFC," Journal of Power Sources, vol. 77, pp. 136–142, Feb. 1999.

[65] A. Albina, P. L. Taberna, J. P. Cambronne, P. Simon, E. Flahaut, and T. Lebey, "Impact of the surface roughness on the electrical capacitance," Microelectronics Journal, p. 7, 2006.

[66] Y. Zhao, G. C. Wang, and T. M. Lu, "Surface-roughness effect on capacitance and leakage current of an insulating film," PHYSICAL REVIEW LETTERS, vol. 60, no. 12, 1999.

[67] L. Daikhin, A. Kornyshev, and M. Urbakh, "Double layer capacitance on a rough metal surface- surface roughness measured by Debye ruler," Electrochimica Acta, vol. 42, no. 19, pp. 2853–2860, 1997.

[68] S. A. Kazaryan, S. N. Razumov, S. V. Litvinenko, G. G. Kharisov, and V. I. Kogan, "Mathematical Model of Heterogeneous Electrochemical Capacitors and Calculation of Their Parameters," Journal of The Electrochemical Society, p. 17, 2006.

[69] M. Laporta, M. Pegoraro, and L. Zanderighi, "Perfluorosulfonated membrane (Nafion): FT-IR study of the state of water with increasing humidity," Physical Chemistry Chemical Physics, vol. 1, no. 19, pp. 4619–4628, 1999.

[70] T. Komura, G. Y. Niu, T. Yamaguchi, and M. Asano, "Redox and ionic-binding switched fluorescence of phenosafranine and thionine included in Nafion films," Electrochimica Acta, p. 9, 2003.

[71] E. Niu, K. Ghiggino, T. Smith, and A. Mau, "ENERGY TRANSFER BETWEEN FLUORESCENT DYES IN ALCOHOLS AND IN NAFION MEMBRANES," Journal of Luminescence, vol. 46, no. 3, pp. 191–199, 1990.

[72] E. Szajdzinska-Pietek, M. Wolszczak, A. Plonka, and S. Schlick, "Structure and Dynamics of Micellar Aggregates in Aqueous Nafion Solutions Reported by Electron Spin Resonance and Fluorescence Probes," vol. 32, no. 22, p. 7, 1999.

[73] D. Weir, "STUDYOF THE EXCITEDSTATES OF NAFION INCORPORATED XANTHONEAND BENZOPHENONE'," p. 7.

[74] Q. Deng, Y. Hu, R. B. Moore, C. L. McCormick, and K. A. Mauritz, "Nafion ORMOSIL hypbrids via in situ sol gel reactions Pyrene fluorescence probe investigations of nanoscale environment," p. 9.

[75] P. C. Lee and D. Meisel, "Photophysical Studies of Pyrene Incorporated in Nafion Membranes," Photochemistry and Photobiology, vol. 41, no. 1, pp. 21–26, 1985.

[76] D. B. Spry and M. D. Fayer, "Proton Transfer and Proton Concentrations in Protonated Nafion Fuel Cell Membranes," p. 12.

[77] S. K. Dishari and M. A. Hickner, "Antiplasticization and Water Uptake of Nafion Thin Films," ACS Macro Letters, p. 5, 2012.

[78] E. S. S. Iyer, D. Samanta, A. Dey, A. Kundu, and A. Datta, "2-(2-Pyridyl)benzimidazole as a Fluorescent Probe of Hydration of Nafion Membranes," J. Phys. Chem. B, p. 7, 2012.

[79] T. Klotzbach, M. Watt, Y. Ansari, and S. D. Minteer, "Effects of hydrophobic modification of chitosan and Nafion on transport properties, ion-exchange capacities, and enzyme immobilization," Journal of Membrane Science, p. 8, 2006.

[80] A. Ryder, S. Power, and T. Glynn, "Evaluation of Acridine in Nafion as a Fluorescence-Lifetime-Based pH Sensor," Society for Applied Spectroscopy, vol. 57, no. 1, p. 7, 2003.

[81] E. P. Kirby and R. F. Steiner, "Influence of solvent and temperature upon the fluorescence of indole derivatives," The Journal of Physical Chemistry, vol. 74, no. 26, pp. 4480–4490, 1970.

[82] M. M. Lee and B. R. Peterson, "Quantification of small molecule–protein interactions using fret between tryptophan and the pacific blue fluorophore," ACS Omega, vol. 1, no. 6, pp. 1266–1276, 2016. PMID: 28058293.

[83] S. H. De Almeida and Y. Kawano, "Ultraviolet-visible spectra of Nafion membrane," European Polymer Journal, vol. 33, pp. 1307–1311, Aug. 1997.

[84] C. Heitner-Wirguin, "Infra-red spectra of perfluorinated cation-exchanged membranes," Polymer, vol. 20, pp. 371–374, Mar. 1979.

[85] C. Korzeniewski, Y. Liang, P. Zhang, I. Sharif, J. P. Kitt, J. M. Harris, S. J. Hamrock, S. E. Creager, and D. D. DesMarteau, "Vibrational Spectroscopy for the Determination of Ionizable Group Content in Ionomer Materials," Applied Spectroscopy, vol. 72, pp. 141–150, Jan. 2018.

[86] S. A. Perusich, "FTIR equivalent weight determination of perfluorosulfonate polymers," Journal of Applied Polymer Science, vol. 120, no. 1, pp. 165–183, 2011.

[87] A. Lachenwitzer, N. Li, and J. Lipkowski, "Determination of the acid dissociation constant for bisulfate adsorbed at the Pt(111) electrode by subtractively normalized interfacial Fourier transform infrared spectroscopy," Journal of Electroanalytical Chemistry, p. 14, 2002.

[88] I. Kendrick, "Operando infrared spectroscopy of the fuel cell membrane electrode assembly Nafion-platinum interface," p. 5.

[89] D. Malevich, J. Li, M. K. Chung, C. McLaughlin, M. Schlaf, and J. Lipkowski, "In situ IR reflectance absorption spectroscopy studies of the effect of Nafion on CO adsorption and electrooxidation at Pt nanoparticles," Journal of Solid State Electrochemistry, vol. 9, pp. 267–276, May 2005.

[90] D. Malevich, V. Zamlynny, S.-G. Sun, and J. Lipkowski, "In situ Infrared Reflection Absorption Spectroscopy Studies of the Interaction of Nafion with the Pt Electrode Surface," Z. Phys. Chem., vol. 217, pp. 513–525, 2003.

[91] M. Falk, "An infrared study of water in perfluorosulfonate (Nafion) membranes," Canadian Journal of Chemistry, vol. 58, pp. 1495–1501, July 1980.

[92] R. Prost, "The Influence of the Christiansen Effect on I.R. Spectra of Powders," Clays and Clay Minerals, vol. 21, pp. 363–368, Oct. 1973.

[93] J. Evans and N. Wright, "A peculiar effect in the infrared spectra of certain molecules," Spectrochimica Acta, vol. 16, no. 3, pp. 352 – 357, 1960.

[94] X. dong Liu, L. tian Hou, and H. tian Wang, "Investigations into the mid-infrared christiansen effect of the dispersive materials," Infrared Physics and Technology, vol. 43, no. 6, pp. 401–405, 2002.

[95] J. A. Dean and N. A. Lange, eds., Lange's handbook of chemistry. McGraw-Hill handbooks, New York, NY: McGraw-Hill, 15. ed ed., 1999. OCLC: 833364385.

[96] "Nafion perfluorinated resin solution." Library Catalog: www.sigmaaldrich.com, accessed: 2020-03-13.

[97] PubChem, "Propanol." Library Catalog: pubchem.ncbi.nlm.nih.gov, accessed 2020-03-13.

[98] R. P. Rossman and W. R. Smith, "Density of Carbon Black by Helium Displacement," Industrial & Engineering Chemistry, vol. 35, pp. 972–976, Sept. 1943.

[99] C. Welch, A. Labouriau, R. Hjelm, B. Orler, C. Johnston, and Y. S. Kim, "Nafion in Dilute Solvent Systems: Dispersion or Solution?," ACS Macro Letters, vol. 1, pp. 1403–1407, Dec. 2012.

[100] R. C. Chiu and M. J. Cima, "Drying of Granular Ceramic Films: II, Drying Stress and Saturation Uniformity," Journal of the American Ceramic Society, vol. 76, pp. 2769–2777, Nov. 1993.

[101] R. C. Chiu, T. J. Garino, and M. J. Cima, "Drying of Granular Ceramic Films: I, Effect of Processing Variables on Cracking Behavior," Journal of the American Ceramic Society, vol. 76, pp. 2257–2264, Sept. 1993.

[102] E. R. Dufresne, E. I. Corwin, N. A. Greenblatt, J. Ashmore, D. Y. Wang, A. D. Dinsmore, J. X. Cheng, X. S. Xie, J. W. Hutchinson, and D. A. Weitz, "Flow and Fracture in Drying Nanoparticle Suspensions," Physical Review Letters, vol. 91, p. 224501, Nov. 2003.

[103] K. B. Singh, L. R. Bhosale, and M. S. Tirumkudulu, "Cracking in Drying Colloidal Films of Flocculated Dispersions," Langmuir, vol. 25, pp. 4284–4287, Apr. 2009.

[104] K. B. Singh and M. S. Tirumkudulu, "Cracking in Drying Colloidal Films," Physical Review Letters, vol. 98, p. 218302, May 2007.